December 2021

Dynamic Mechanical Behaviors of Nacre-Inspired Graphene-Polymer Nanocomposites Depending on Internal Nanostructures

Cho Chun Chiang
Clemson University, crazame@gmail.com

DYNAMIC MECHANICAL BEHAVIORS OF NACRE-INSPIRED GRAPHENE-POLYMER NANOCOMPOSITES DEPENDING ON INTERNAL NANOSTRUCTURES

A Thesis
Presented to
the Graduate School of
Clemson University

In Partial Fulfillment
of the Requirements for the Degree
Master of Science
Mechanical Engineering

---

by
Cho-Chun (Jonathan) Chiang
December 2021

Accepted by:
Dr. Zhaoxu Meng, Committee Chair
Dr. Qiushi Chen
Dr. Zhen Li
Dr. Huijuan Zhao

Abstract

Nacre, a natural nanocomposite with a brick-and-mortar structure existing in the inner layer of mollusk shells, has been shown to optimize strength and toughness along the laminae (in-plane) direction. However, such natural materials more often experience impact load in the direction perpendicular to the layers (i.e., out-of-plane direction) from predators. The dynamic responses and deformation mechanisms of layered structures under impact load in the out-of-plane direction have been much less analyzed. The optimal design of protective material systems by leveraging the bioinspired structure has not yet been achieved. The main objective of this thesis is to investigate the dynamic mechanical behaviors of nacre-inspired layered nanocomposite films under impact in the out-of-plane (i.e., thickness) direction by using a model system that comprises alternating multilayer graphene (MLG) and polymethyl methacrylate (PMMA) phases.

With a validated coarse-grained (CG) molecular dynamics simulation approach, my thesis systematically studies the mechanical properties and impact resistance of the MLG-PMMA nanocomposite films with different internal nanostructures, which are characterized by the layer thickness and the number of repetitions while keeping the total volume constant. As the layer thickness decreases, the effective modulus of the polymer phase confined by the adjacent MLG phases increases. This observation demonstrates that the adopted CG models capture the nanoconfinement effect on the polymer phase. I then use ballistic impact simulations to explore the dynamic responses of nanocomposite films in the out-of-plane direction. I find that the impact resistance and dynamic failure

mechanisms of the films depend on the internal nanostructures. Specifically, when each layer is relatively thick, the nanocomposite is more prone to spalling-like failure induced by compressive stress waves from the projectile impact. Whereas, when there are more repetitions and each layer becomes relatively thin, a high-velocity projectile sequentially penetrates the nanocomposite film. In the low projectile velocity regime, the film develops crazing-like deformation zones in PMMA phases. Such crazing-like deformation is believed to dissipate the energy and delocalize the concentrated impact loading effectively. Furthermore, I find that the position of the soft PMMA phase relative to the stiff graphene sheets plays a significant role in the ballistic impact performance of the investigated films.

In summary, this thesis provides insights into the effect of nanostructures on the dynamic mechanical behaviors of layered nanocomposites under impact loading along the thickness direction. The revealed dependence and underlying deformation mechanisms can lead to effective design strategies for impact-resistant films.

Acknowledgements

First and foremost, I would like to express my sincerest gratitude to my advisor, Dr. Zhaoxu Meng, for his continuous support of my Master's thesis study with great patience, motivation, and encouragement. His guidance has helped me to develop my academic and research skills, and more importantly, to become a critical and independent researcher. I have been imperceptibly influenced by his passionate and rigorous academic behavior, which will be a great treasure in my future life.

Besides my advisor, I would like to thank the rest of my thesis committee members: Dr. Huijuan Zhao, Dr. Qiushi Chen, and Dr. Zhen Li, for their insightful comments and inspiring questions, which stimulated me to enhance my thesis research from various perspectives. I value the knowledge learned from the classes of Dr. Zhao, which helped me to establish a firm foundation on solid mechanics. I also appreciate the precious research experience collaborating with Dr. Chen. His meticulous working attitude has significantly enhanced my critical thinking skills when doing research. I am grateful for his constructive challenges to my work. Additionally, I would like to thank Dr. Li for serving as one of my thesis committee members and provide valuable feedback on my oral defense.

During the two years of my Master study, I have been financially supported by the appointment of assistantship from our Department of Mechanical Engineering. I was able to sustain my own living and the Master study at Clemson. I would also like to thank for the generous allotment of computational time on the Palmetto cluster. Without the financial

support and the computational resources from Clemson, I would not be able to complete my research. These sources of support are gratefully acknowledged.

Finally, I would like to express my gratitude to my family. My parents, aunt, and grandparents have been supporting me spiritually throughout my entire oversea academic life. Thanks to their reliable supports, I can therefore finish my Bachelor's degree at Hong Kong, and eventually complete my Master study here in the United States. I am also truly thankful to my siblings for their backing and guidance in my life. Their support throughout the Master study, as well as my entire life, has shaped me as who I am today; and I cannot feel more grateful to that.

I am overwhelmed to all the wonderful people in my life who have ever supported me or witnessed my growth up till this moment. Deep dept of gratitude is noted here but far beyond words.

Table of Contents

List of Figures

List of Tables

Chapter 1 Introduction

1.1 General background

Developing impact-resistant films or barriers is a fast-growing research area as researchers are looking for an effective protective means in multiple applications. For instance, it is crucial for military and aeronautic applications as resisting impact and dynamic load is imperative to the functionality, especially when human safety becomes a concern [1-3]. Another area of high importance is protective and shielding devices used in microelectronics, which may undergo accidental shocks during the service lives [4, 5]. There have been significant developments in commercial protective gears as well, including vehicle's windshield, protective gears for sports [6, 7], and in the military and aeronautic industry [2, 8-11]. In such developments, theoretical models for protective layered composites have been constructed to describe the mechanical response under high strain loading [12, 13]. Despite advancements in traditional protective materials systems, one can expect significant or even revolutionary improvements in next-generation protective materials by integrating advanced nanomaterials and judiciously designed nanostructures [14].

It has been recognized that materials with feature sizes of nanometers exhibit unique properties compared to their macroscopic counterparts. Such behaviors can often result from the quantum size effect or the surface effect when the materials scale down to nanoscale [15-18]. The Quantum size effect describes the different behaviors that electrons

have at different scales and can be best illustrated in semiconductor applications, in which the electrical conductivity varies depending on the size-dependent delocalization property of the electrons [15, 19-21]. On the other hand, the surface effect influences the surface-to-volume ratio of the materials. With an increased surface area, it leads to a higher average binding energy per atom, which can significantly affect the mechanical or electrochemical properties of the materials [15, 22, 23]. For instance, metallic systems in nanometer size can achieve theoretical strength limits [24, 25] and metals with nanocrystalline grain structure also possess enhanced thermal-mechanical properties [26-29]. Similar behaviors can also be observed on the dynamic response of the materials in protective applications under impact load. A recent study demonstrated that nanometer-thin multilayer graphene (MLG) sheets have specific penetration energy ten times larger than bulk steel on an equal weight basis using novel microprojectile impact tests [30]. Moreover, ultrathin (less than 100 *nm*) polymer films have unique physical properties compared to their bulk counterpart [31-39], in which the viscoelastic mechanism can have a huge difference between a nanoscale MD simulation result and a larger scale experimental result [40, 41]. Another recent study found that semicrystalline polymer thin films achieve higher specific penetration energy than bulk protective materials and previously reported nanomaterials [31]. The reason was also attributed to the effective strain delocalization during impact and the abundant viscoelastic and viscoplastic deformation mechanisms within the polymer thin films. These findings all illustrate the importance of studying and designing a protective thin film from a nanoscale perspective.

Designing nanocomposites with unique nanostructures is a promising strategy to equip material systems with excellent impact resistance and protective capability. In this regard, natural biomaterials provide great inspiration for the nanostructure and hierarchical structures that usually combine a stiff, robust phase and a soft, dissipative phase. Various hierarchically structured biomaterials have demonstrated mechanical properties surpassing those of the individual constituents by orders of magnitude [42-44]. The Bouligand structure, found in crustacean and beetle exoskeletons [45-47], fish scales [48, 49], and mantis shrimp dactyl clubs [50], have been shown to exhibit high impact tolerance and strength [51]. Previous work has revealed the unique role of nanostructural features in the impact resistance of Bouligand films made from high aspect ratio nanofibers [51]. Another widely studied natural material - nacre, the inner layer of a mollusk shell - features layered arrangements of hard and soft phases forming a brick-and-mortar type of structure. It is known to be an outstanding example that has high specific strength and toughness [52, 53]. By imitating its multilayer structure arrangement in nanoscale, structural materials with high mechanical performance can be fabricated [54-57]. Mechanical properties of the nacre-inspired nanocomposites have been studied widely using experiments [55, 56] and simulations [35, 57, 58]. Experiments have shown the outstanding stiffness and fracture toughness contributed to the nacre-like layered structure [55, 56]. Computational studies, particularly molecular dynamics (MD) simulations, have also been applied to analyze the mechanisms underlying the excellent mechanical properties of such nanocomposites.

Recent studies have also shown that the nanoconfinement effect on the (bio)polymer phase by the adjacent stiffer layers plays a role in the enhanced mechanical

property of materials with nacre-inspired structures [35, 59, 60]. Specifically, the nanoconfinement effect increases the strength, toughness, and interfacial interaction strength of the polymer phase within the thin nanocomposite films [35, 60]. Although the in-plane mechanical properties of the nacre-inspired nanocomposites have been widely studied, the out-of-plane mechanisms of these nanocomposites have yet to be fully understood. These mechanisms are directly relevant to the design of nanocomposites that can possess excellent impact resistance.

This thesis thus attempts to understand the dynamic response of nacre-inspired nanocomposite films under ballistic impact in order to study their out-of-plane behavior. The studied nanocomposite systems are comprised of hard phases - MLG sheets - and soft phases - polymethyl methacrylate (PMMA). The systems adopt a layered structure with changing layer thickness while conserving the total system volume. A previously developed coarse-grained (CG) model of MLG and PMMA used in molecular dynamics (MD) simulations [61, 62] is utilized. These models have been validated to capture the mechanical properties and failure behaviors of both MLG and PMMA [57, 59, 63-67]. The models are able to characterize the failure mechanisms that influence the toughness and energy dissipation of the system. Particularly, the interfacial sliding between the graphene sheets has a great influence on the toughness of the system and is shown to have different modes of failure depending on how the MLG structure is staggered [57]. On the other hand, a previous study utilizing the CG model also found out that energy dissipation of the system can be enhanced by increasing the interfacial strength between the MLG and PMMA [57]. Moreover, it is also shown that with a specific wrinkle MLG configuration inserted in MLG

reinforced nanocomposites, such interfacial sliding between graphene sheets can result in a rising level of energy dissipation. These findings illustrate a direct advantage with regard to a better energy dissipation of the system contributed to nacre-like layered nanostructure [65]. Facilitating the capability and advantage of this model has on characterizing the failure mechanism, particularly the interfacial behaviors between graphene-graphene and MLG-PMMA, my thesis will focus on using these CG models to study the dynamic failure behaviors of MLG-PMMA nanocomposites by conducting ballistic impact simulations and provide insights into the nanoscale ballistic response of individual nanoscale thin films [68-70].

1.2 Scope & objectives

The research efforts of capturing and understanding the mechanical response of various kinds of nacre-inspired nanocomposite have been on the rise recently. Numerous research has studied the in-plane mechanical property of such material already. Although a few attempts have been made on studying the ballistic performance of different layered nanocomposites using atomistic scale MD simulation in recent studies, most of them have restrictions on analyzing a larger scale system due to the limitation of computational resources or have different arrangements of the layered nanostructure. The questions then arise as: (1) how to accurately characterize the dynamic failure mechanism of the MLG-PMMA nanocomposites using the CG-MD model; (2) how do different nanostructure arrangements affect the mechanical properties or the dynamic response of the material under ballistic impact; (3) what are the mechanisms that this nanocomposite material exhibit to absorb and dissipate the induced kinetic energy during the perforation process?

By addressing these questions, the main objective of my thesis is to characterize the dynamic mechanism of the nacre-inspired MLG-PMMA nanocomposites under ballistic impact simulation using the previously validated CG-MD model. Revolving this objective, the main study of this thesis will be to conduct ballistic impact simulation on the material. The specific tasks include:

1. An extensive literature review of current approaches that studies ballistic impact simulation with high impact velocity on ultrathin nanocomposites film in MD simulation.
2. To design tensile and nanoindentation testing simulations for characterizing the in-plane mechanical properties of different nanostructure systems.
3. To design and investigate the dynamic response and failure mechanisms of different systems under high-velocity impact using two different shapes of the projectile to verify the consistency of the ballistic performance of the systems.

1.3 Thesis organization

This thesis is organized into four chapters. The introduction is presented in Chapter 1, followed by Chapter 2 that presents the MD and CG-MD basics and review. The main chapter (Chapter 3) is the related research topic, which has been published in technical journals [67]. The summary of this main chapter is listed as follows:

Chapter 3 presents a systematic comparison to characterize the ballistic performance of nanocomposite systems with different nanostructure arrangements. Extensive studies have been done to show the possibility of tailoring material's impact

resistance through manipulating its layered structure layout. I particularly focus on the energy dissipation and deformation mechanisms during impact wave propagation. The findings in these aspects provide fundamental insights into effective design strategies of protective thin films.

As a conclusion of this thesis, Chapter 4 summarizes the main findings of this thesis, discusses the limitations of the current work, and outlines the possible directions of future research.

Chapter 2 Molecular Dynamics Simulation Basics and Review

2.1 Overview

Molecular Dynamics (MD) is a computer simulation technique that is particularly suitable for analyzing the physical movements and collective behaviors of atoms and molecules. It predicts the interaction of a particular system, in which atoms and molecules are permitted to interact for a certain time period and therefore provides a view of how the system behaves dynamically along with the time evolution. The predictions of the generation of the atomic trajectories of a system are typically determined by numerically solving Newton's equation of motion. Such Newtonian forces between atoms or molecules are defined and calculated using prescribed interatomic potential and boundary conditions.

MD was first developed as a tool to exploit computing machines during World War II, which follows the earlier successes with Monte Carlo simulations. However, it was not popularized until 1952 at Los Alamos National Laboratory, which studied statistical mechanics in what is known today as the Metropolis Monte-Carlo algorithm using the MANIAC computer [71]. The first MD simulation was conducted in 1957 to study a solid-fluid transition in a system composed of hard spheres interacting by instantaneous collisions [72]. The simulation consisted of 500 particles and took approximately an hour to complete on an IBM 704 computer. Nowadays, MD has been significantly advanced and

become a general technique to investigate all kinds of systems and to simulate the problems in a variety of different engineering branches.

MD exhibits several advantages. First, MD simulations can usually be set up easily. The involved potential field of the investigated system can generally be derived through various developed models. Once the system is built, the force acting on every atom is obtained by such deriving equations, which significantly accelerate the process as it can be applied to all the simulations in the research. Second, MD simulations are generally cheaper comparing to physical experiments that require costly equipment and specimens. The major drawback of MD is also obvious. As MD tracks the interactions and motions of all particles, MD simulations are quite computationally expensive, which makes it difficult to scale up. Nevertheless, with the advent of computer hardware and parallel capabilities (i.e., high performance computing cluster), the MD has become one of the most powerful numerical tools that can provide valuable information of and shed light upon the nanoscopic behavior of molecular systems, which is often difficult or impossible to obtain from physical experiments.

2.2 Key components of MD

This section will discuss the basic elements required to run a typical MD simulation. Section 2.2.1 provides a basic understanding of the particle structure. In which the particle-to-particle force interaction is discussed in Section 2.2.2. The following sections (Section 2.2.3 – 2.2.5) then represent the typical numerical solution and procedure to solve the motion of the particle in MD simulations.

2.2.1 Particle structure

In general, MD simulation is a tool to study the physical movement of a particle structure. Particle structures are usually representations of atoms or molecules, which the force interaction between each particle is described by an implemented potential field. Particle structures are normally configured with detailed information of the particles, such as the position of the atoms, the bond connection between two atoms, and the angle between two bonds. Particles in the structure have mass, and their physical movement, such as position, velocity, and acceleration, are always tracked during an MD simulation. System box boundaries are also introduced in an MD simulation when generating particle structure. They may be periodic or fixed (non-periodic). Periodic boundaries produce duplicated images through the specified domain, whereas fixed boundaries generate a single image only. Duplicating the particle structure can greatly reduce the computational resource demand as only the original kernel needs to be simulated.

2.2.2 Empirical potential

The potential function is a crucial factor in an MD simulation. It describes the terms of how the particles in the simulation will interact. Such potential functions are often referred to as a force field in chemistry and bio-molecules or as an interatomic potential in material science. The interatomic potential is usually defined based on classical mechanics to reproduce the structural and conformational changes within particle-to-particle interactions. It can be generated by fitting experimental data of the studied material and the first-principles method.

Most typical potential force fields are associated with bonded (i.e., pairs, angles, and dihedrals) and non-bonded (i.e., van der Waals, electrostatic, and more) forces. These potentials contain free parameters such as the radius of the atom, the bond angle within two bonds, or the adhesion energy of the structure surface. Such parameters can be obtained by fitting detail quantum-mechanical and quantum-chemical simulations like Density-Functional theory (DFT); or through experimental physical properties such as modulus of elasticity and stiffness. The total potential energy of the material is simply the sum of all potential energies of pairs of atoms. Depending on what the study focuses on, different defined potential forces may be proposed by excluding the negligible potential part for the same material.

Multiple empirical potentials have been developed and proposed. For instance, reactive potential AIREBO [73] or ReaxFF [74] for studying hydrocarbons; Tersoff potential for studying silicon and carbon [75, 76]. These various force field potentials serve as a convenient tool for future researchers to investigate the materials without having to calibrate the empirical potential.

2.2.3 Newton's equations of motion

In MD, the motion of particles is described by numerically solving Newton's equations of motion. For any particles in the simulation system, Newton's equations of motion are written as

$$F_i = m_i a_i \tag{2.1}$$

where F_i is the overall interatomic force interaction that is described by the potential field; m_i is the mass of the particle; a_i is the translational acceleration of the particle. The force can also be expressed to the negative gradient of potential U with respect to the position

$$F_i = -\nabla_i U \tag{2.2}$$

Combining Equation (2.1) and (2.2) yields

$$-\frac{dU}{dr_i} = m_i a_i = m_i \frac{dv_i}{dt} = m_i \frac{d^2 r_i}{dt^2} = \frac{dp}{dt} \tag{2.3}$$

where r_i is the position; v_i is the velocity; p is the momentum of the particle, and t is the time. Newton's equation of motion can then relate the derivative of the potential energy to the changes in position as a function of time. Therefore, with the prescribed potential U, the position r, velocity v, momentum p, and acceleration a can be evaluated. Note that in order to solve the motion of each particle, all the forces taking roles in the interaction need to be evaluated and summed, including but not limited to the potentials mentioned in the previous section (Section 2.2.2).

2.2.4 Time integration algorithm

To fully obtain the particle motion governed by Equation (2.3) that involves the time integration scheme, a proper numerical tool must be introduced. There are multiple time integration algorithms, in which the second-order Velocity-Verlet algorithm [77] is commonly adopted in the calculation and is explained in this section as a sample algorithm.

Velocity-Verlet algorithm keeps track of one vector of position and one vector of velocity. Assuming the current state of the particles is indexed by time t and the time

increment to the next state is Δt, the algorithm will first calculate the velocity at $t + \Delta t/2$ by

$$\vec{v}\left(t + \frac{1}{2}\Delta t\right) = \vec{v}(t) + \frac{1}{2}\vec{a}(t)\Delta t \tag{2.4}$$

where *v* is the particle velocity, and *t* indicates the time index of the state of such particle. The position of the particle can be calculated as

$$\vec{r}(t + \Delta t) = \vec{r}(t) + \vec{v}\left(t + \frac{1}{2}\Delta t\right)\Delta t \tag{2.5}$$

where *r* is the position of the particle. Deriving $\vec{a}(t + \Delta t)$ using $\vec{r}(t + \Delta t)$ in Equation (2.5) and compare it with Equation (2.4) updates the velocity as

$$\vec{v}(t + \Delta t) = \vec{v}\left(t + \frac{1}{2}\Delta t\right) + \frac{1}{2}\vec{a}(t + \Delta t)\Delta t \tag{2.6}$$

This derivation makes Velocity-Verlet algorithm a numerically stable approach as it has implicit characters. The velocity determined by such an algorithm requires factorization of the accelerations at that time index, which has a feedback effect on the position. Unlike explicit integration algorithms, the quantities at a successive time in the Velocity-Verlet algorithm do not solely depend on that at a previous time, allowing the systems not to escape.

However, timestep (time increment) is a key factor in all algorithms, even for implicit integration algorithm. The value will have to be small enough to achieve numerical stability during calculation, which will be discussed in Section 2.3.

2.2.5 Computational procedure

MD simulations require reiteration during the process, similar to other numerical tools. Figure 2.1 shows and summarizes the procedure and calculations that are involved in one typical iteration of an MD simulation.

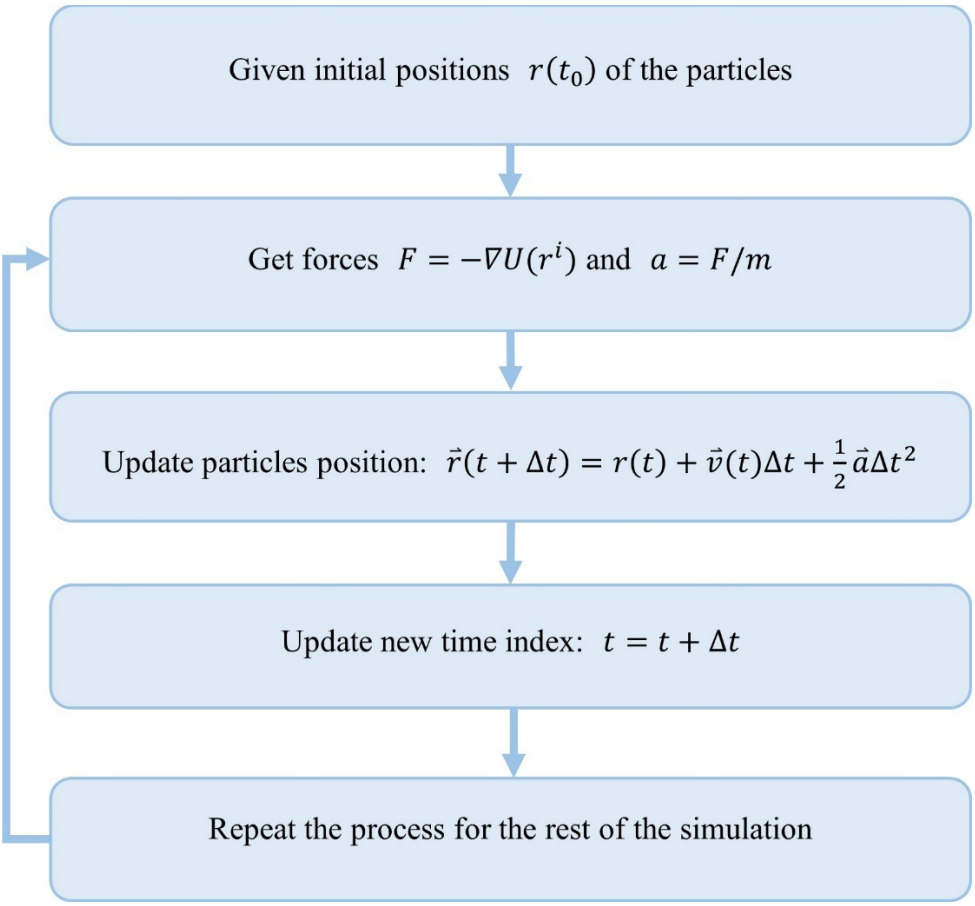

Figure 2.1: The workflow and calculations that are involved in a typical MD simulation.

2.3 Coarse-grained molecular dynamics (CG-MD) simulation

2.3.1 Overview

One of the major drawbacks of an atomistic MD simulation is its limitation to simulate physical processes at a longer temporal or a larger length scale [78]. Because of the numerical stability an MD simulation needs to achieve during the iteration, the value of the timestep is usually extremely small. Typical MD simulations use one femtosecond (*fs*) as their timestep, which makes it computationally expensive for a larger system or a diffusive process. Several solutions have been proposed to reduce the computational cost of MD simulations, and one of the most effective ones is by coarse-graining the system.

Coarse-grained (CG) models have become more popular in recent years as a tool to resolve the scale issue an MD simulation has. It simplifies the system by clustering groups of particles (i.e., atoms or molecules) into newly defined CG beads. This strategy reduces the degree-of-freedom of the original system, resulting in a simplified representation of the system. CG-MD has been widely employed to study a variety of problems, such as the lipid membranes made of graphene nanosheet and the backbone structure of different polymers [61, 79]. For instance, the MARTINI model is one of the most popular models for studying lipids, surfactants, or proteins [80, 81]. The model clusters four heavy atoms to a single interaction bead representation. Therefore, a typical protein structure can have its backbone unit simplified to one bead and side group to one or more beads, which results in fewer representations comparing to that of all atomistic structures [80]. Similar to an all-atomistic MD simulation, new CG beads interact through an effective potential field. The MARTINI

model defines four basic interactions: polar, nonpolar, apolar, and charged. Each basic interaction can be further divided into several subtypes to precisely capture the force interactions. This key feature provides flexibility as no built-in restrictions exist to the phase of the system, allowing the model to be easily extended to model different biomolecules [80]. Multiple models has been proposed for various CG structures [61, 80, 82-84], which offer great promises as they make simulating mesoscale problems while retaining the molecular detail of the system possible.

2.3.2 Coarse-grained model of MLG-PMMA structure

In my thesis study, a previously developed CG model for the investigated structure, multilayer graphene (MLG)-PMMA, has been utilized to study the structure's dynamic failure mechanism. The construction of the nacre-inspired nanocomposite films is configured with the brick-and-mortar structure of alternating MLG and PMMA phases using the CG models of MLG and PMMA. The CG model of the MLG sheets employs a 4-to-1 mapping scheme that conserves the hexagonal symmetry [62]. This model has been shown to capture the anisotropic mechanical response and orientation-dependent interlayer shear behavior of MLG [62]. The CG model of the PMMA adopts a two-bead mapping scheme for each monomer, in which one represents the side chain methyl group and the other one represents the backbone group [61]. This CG model captures the thermal and mechanical properties of the PMMA, including the ones that emerged from nanoscale thin film configurations [35, 39]. Such a CG model requires significantly lower computational cost comparing to that of the all-atomistic structure of the same system. Depending on the simulation setup, the CG model can potentially have an increase of up to 2 orders of

magnitude in computational speed [62]. In which a timestep value of 4 *fs* can be generally achieved without losing the model's stability. However, a smaller timestep value ranging from 1 to 4 *fs* is used in this research, specifically during high-velocity impact simulations so that more detail of the dynamic failure mechanism is retained for observation; the enhancement in computation efficiency of this CG model is not focused in this thesis.

It is further noted that the CG model of PMMA in this research does not include bond-breaking criteria in the system, which, however, can be easily included in future studies if such criteria are needed. A previous study has shown that the dominant failure mechanisms of PMMA films consisting of only short chains under ballistic impact are the interchain pull-out or disentanglement, and bond stretching in the polymer chains is not significant [57]. Overall, the utilized CG model of MLG-PMMA nanocomposites has been validated by testing the model performance in different problems, such as tensile test, interlayer shearing test, and steered molecular dynamics pulling test [57, 65]. The test results show the capability of this CG model in simulating complex mechanical physics problems with satisfying molecular details retained.

The potential field of the CG model follows a similar approach to a typical MD simulation, in which the conservation of the total potential energy is considered. The total potential energy includes the contributions from bonds, angles, dihedrals, and non-bonded interactions of graphene nanosheet and PMMA systems. Free parameters are then being calibrated and obtained by fitting the value from experiment or simulation results. A more detailed discussion on the calibration of the potential field of this CG model can be found in the work of Ruiz [62] and Hsu [61].

2.4 Summary

A brief review of MD simulation and the corresponding CG model for the investigated nanocomposites in this research has been presented in this chapter. A general MD simulation involves the following components: particle structure, potential field, Newton's equation of motion, and a time integration algorithm (i.e., Velocity-Verlet algorithm). The importance of the small value of timestep in order to maintain numerical stability during the calculation has been discussed. A workflow of a typical MD simulation has also been described.

This chapter also presented the configuration of the utilized CG model for MLG-PMMA nanocomposites. The model has been shown to greatly reduce the computational cost comparing to that of an all-atomistic model while retaining satisfied molecular detail for analysis. A brief comparison between MD and CG-MD simulation has also illustrated the importance of such a CG model, which allows the study of high-velocity impact tests on the nano-thin film.

Similar to atomistic level potential fields, the parameters in the potential field of this CG model are difficult, if not impossible, to be directly measured from physical experiments. A calibration process is therefore needed to obtain an accurate potential field that adequately captures the targeted properties of the model system. A brief description of the approach for model calibration has also been summarized in this chapter.

Chapter 3 Characterizing Behaviors of MLG-PMMA Nanocomposites using CG-MD Simulations

3.1 Overview of the coarse-grained model setup

The investigated system consists of alternating MLG and PMMA phases with designed thickness, and one repetition module includes an MLG phase and a thin PMMA film. The number of repetitions (n) is adjusted to conserve the total volume of the nanocomposites, which have 26 layers of graphene sheets and 24 *nm* thick of the PMMA phase in total. The repetition modules (MLG + thin PMMA film) are stacked in a repetitive manner, and the schematic diagrams of the investigated structures are shown in Figure 3.1. Specifically, each repetition module contains N layers of graphene sheets, where $N = 24/n$, and PMMA film with a thickness of $24/n$ *nm*. The system is then being capped with an additional two layers of graphene sheets at the bottom surface, therefore, equaling 26 layers of graphene sheets in total. The PMMA phases consist of blocks of polymer chains with a chain length of 100 monomers per chain.

For simplicity and clarity, the terminology of the different systems is designed based on the position and the number n of the repetition modules of the system. 'Gra' is used to illustrate the default setting where the thicker MLG ($N \geq 2$) is on top, indicating

that they will be impacted first during the ballistic impact simulations. In Figure 3.1, the number following Gra is the number of repetitions - *n*. Alternatively, PMMA(*n*) is used to illustrate the setting that the cap bilayer graphene sheets and the adjacent PMMA phase experience the impact first. As most of the nanocomposite films studied are not symmetric based on the central plane, these notations enable this thesis to describe the impact responses with projectile impact from both directions. Whereas the Gra12 system is symmetric to the central plane of the film as bilayer graphene sheets are separated by 2 *nm* thick PMMA films. As a result, Gra12 is identical to the notation of PMMA12.

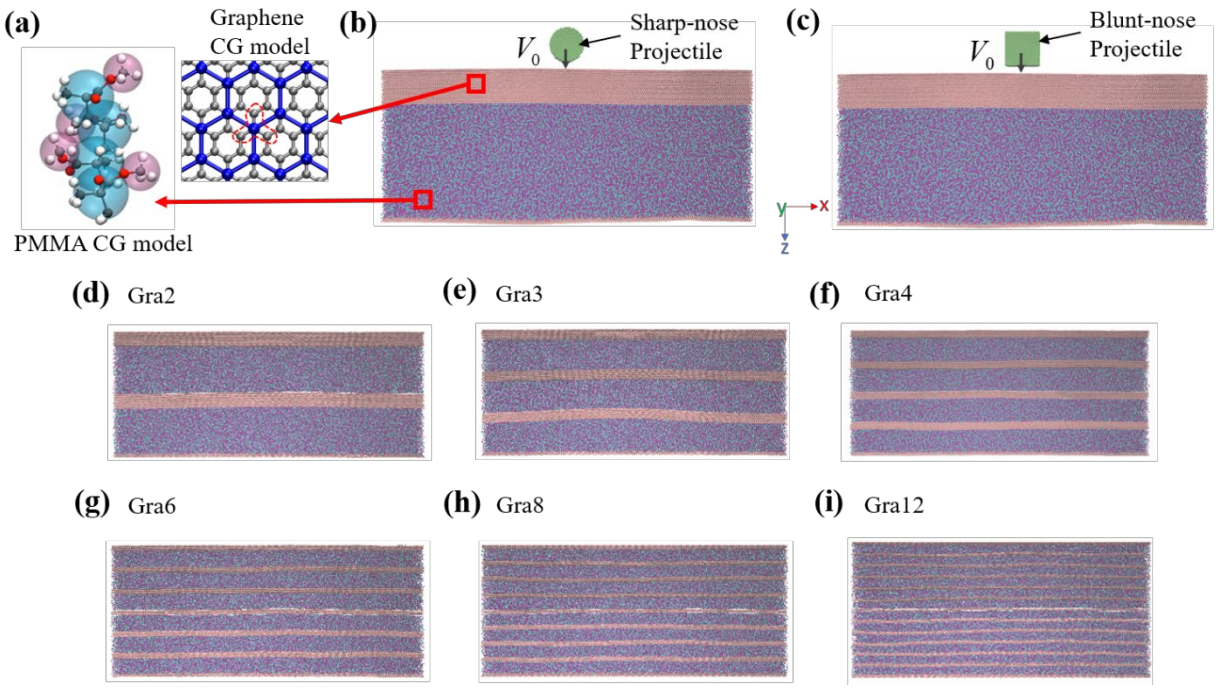

Figure 3.1: (a) Schematics of the CG models utilized in this study and nacre-inspired nanocomposite films with different numbers of repetitions in (b)-(i). The schematics of impact simulation with a (b) sharp-nosed projectile and a (c) blunt-nosed projectile are also shown in the Gra1 film. All systems share the same coordinate.

The total length of the system (along y-direction) is approximately 85 *nm*, and the width of the system (along x-direction) is 42 *nm*. Periodic boundary conditions are applied at both x- and y-directions. Because of this, only a side view of the systems is usually showed in the figures throughout the entire thesis. Vacuum spaces are introduced at both the upper and lower end of the box along z-direction to isolate the nanocomposite system for analysis in this study.

3.2 CG-MD simulation protocols

All the simulations are carried out using the Large-scale Atomic/Molecular Massively Parallel Simulator (LAMMPS) molecular dynamics package [85], and the simulation trajectories are visualized using the Visual Molecular Dynamics (VMD) software [86]. The system is first equilibrated using an NVE ensemble with a Langevin thermostat at 300 *K* for 0.2 *ns*. Then, an annealing process is conducted using direct heating and cooling down under the NPT ensemble throughout the entire process. This entire equilibrium process is conducted in a total period of 1.2 *ns*. It is done by first equilibrating the system at 300 *K* for 0.2 *ns* and then heating it up to 600 *K* within 0.2 *ns*. After the system has reached 600 *K*, it is further equilibrated at such temperature for another 0.2 *ns* to allow the prestress within the PMMA layer to fully relax. 600 *K* is well beyond the glass transition temperature (T_g) of PMMA - 380 *K* as measured in the previous study [57]. Finally, the system is cooled down to 300 *K* using 0.2 *ns* and stays at 300 *K* for 0.4 *ns*. To maintain a stable layered structure during the process, constraints have been added to both ends of the graphene sheets along x-direction to their initial positions by applying a tethering force to the graphene beads in the end regions. The tethering force on both ends

of the graphene sheets resembles the clamped boundary conditions used in experiments. Such constraints are applied to not only maintaining a uniform layered structure during the equilibrium process, but also serving as fixed boundary conditions when the film is impacted by the projectile in the subsequent simulations. The equilibration procedures resemble our previous studies [57, 70], in which the results keep track of the potential energy of the overall investigated structures to ensure the materials are well equilibrated before deformation or projectile impact is conducted. Figure 3.2 (a) and (b) show the potential energy of Gra1 and Gra12 films during the final equilibration stage, which equilibrates the systems by maintaining a constant temperature at 300 *K*. The potential energies of the systems reach a plateau during this relaxation process, indicating fully equilibrated and relaxed systems.

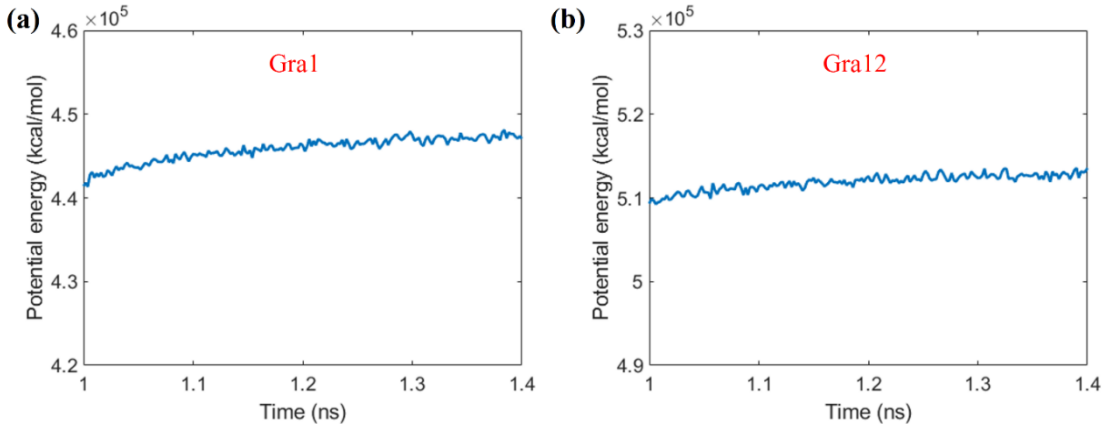

Figure 3.2: The potential energy evolution during the last stage of the equilibration process of (a) Gra1 and (b) Gra12 against time.

After equilibration, three types of non-equilibrium MD (NEMD) simulations, including uniaxial tensile deformation, nanoindentation, and ballistic impact simulations,

are carried out in this study. The uniaxial tensile simulations adopt a constant-strain-rate deformation along the x-direction of the system (See Figure 3.3). The strain rate is $5\times10^{8}/s$, similar to previous studies using MD simulations [35, 87]. Uniaxial tensile simulations are used in order to explore the elastic modulus of the films along the in-plane direction and the nanoconfinement effect from MLG on the PMMA phase. To better understand the in-plane stiffness of the system, nanoindentation simulations are designed in this study. The simulations apply an implicit indenter using the command provided in LAMMPS (see Figure 3.3 (a)). Specifically, a cylindrical shape indenter with a radius of 0.3 *nm* and length along y-direction equaling to the system's width is applied to press downward on the target surface (i.e., indenting in the z-direction). The indenter was then removed after reaching a certain depth, allowing the film to vibrate freely without interference. The free vibrating frequency of the investigated film was then measured by tracking the z-displacement at the centroid of the film. Different indent depths were tested to ensure that the vibrating frequency keeps as constant. The film vibration frequency also allows us to analyze the dependence of mechanical properties of the nanocomposite films on their nanostructures.

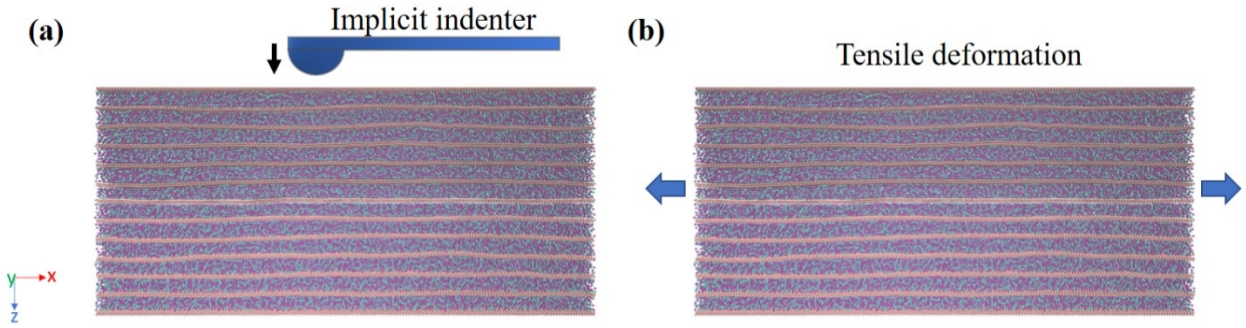

Figure 3.3: Schematic diagrams for (a) nanoindentation and (b) uniaxial tensile testing on the Gra12 film. The nanoindentation simulation consists of an implicit indenter indenting on the film, then removed after it reaches a certain indent depth, allowing the film to vibrate freely. The tensile testing simulation applied an increasing strain with a constant strain rate of $5\times10^{8}\ s^{-1}$ along the in-plane direction of MLG (x-direction).

Lastly, impact responses and dynamic mechanical behaviors of the MLG-PMMA nanocomposites are investigated. High-velocity impact tests with both block- and cylindrical-shape projectiles (shown in Figure 3.1) are performed on the systems to understand their responses under high strain rate loading. The block shape represents a blunt-nosed projectile, and the cylindrical shape is used as a sharp-nosed projectile. The projectiles are comprised of beads in a diamond lattice with the mass of the beads of 96 *g/mol* and a lattice parameter of 0.72 *nm*. The density of the projectiles is approximately 3.4 g/cm^3. Both projectiles are periodic along the y-axis. The blunt-nosed projectile has a square shape at the x-y plane with a width of 8 *nm*. The sharp-nosed projectile has a cylindrical shape with a radius of 4.53 *nm*, which leads to the same mass as that of the block projectile. According to the outcome of previous experiments [30], the projectile shows no observable deformation. Therefore, the projectile is treated as a rigid body in the

impact simulations. In this CG model, 12-6 LJ potential with $\varepsilon_{LJ} = 0.813\ kcal/mol$ and $\sigma_{LJ} = 0.346\ nm$ is used to describe the interactions between the projectile and the graphene and PMMA beads. A previous study about the development of this CG-MD model uses the same parameters of the LJ potential, and it has shown that the interaction between the projectile and film does not significantly affect the impact response [25]. After the equilibration process of the system, a downward impact velocity, V_0, normal to the x-y plane, is assigned to the projectile to initiate the impact process. Projectiles are initiated to impact both the top and bottom surfaces of the nanocomposites, as the nanocomposite film is not symmetric to its central plane. For brevity, the Gra(*n*) films are renamed to PMMA(*n*) when the projectile first impacts the bilayer graphene cap, as the thicker PMMA phase is closer to the strike-face. This thesis systematically analyzes the deformation processes of the nanocomposite films from the trajectories under NEMD simulations.

3.3 Results and discussions

3.3.1 Nanoconfinement Effect

Results from uniaxial tensile simulations are first presented, which characterize the elastic properties of different nanocomposite films along the in-plane direction. Figure 3.4 shows typical stress-strain relationships during the tensile deformation of nanocomposites with different repetition numbers (*n*). The mechanical responses of the entire system are presented in Figure 3.4(a), in which three typical structures are compared. Even though only show three systems are showed for better clarity, it is confirmed that the other

structures show a similar trend. There is an increasing trend of the elastic modulus with increasing *n*. Specifically, Young's modulus of Gra12 rises more than 5% compared to the Gra1 structure. Even though it seems that this is a minor increment, considering the large volume fraction of the graphene phase, which is also a constant for all the systems here, this is still a non-negligible increment in the elastic modulus of the nanocomposites herein. The increase of the elastic property indicates the nanoconfinement effect on the PMMA phase from the adjacent graphene sheets. The nanoconfinement effect is further illustrated by comparing the stresses that originated from the polymer phase only, as shown in Figure 3.4(b). With a decrease in thickness on each PMMA phase (i.e., increasing *n*), both the elastic modulus and general stress levels at the given deformation of the PMMA phase increase, indicating a stiffer and stronger behavior. The observation of the significant difference between Gra1 and Gra12 agrees with previous studies that the elastic moduli of polymer thin films are enhanced by the nanoconfinement effect, which can be tuned by increasing cohesive interaction between polymer and graphene sheets or other substrates [33, 35, 39, 59]. Additionally, the nanoconfinement effect can be tuned by changing the thickness of polymer films under confinement [34, 36-38].

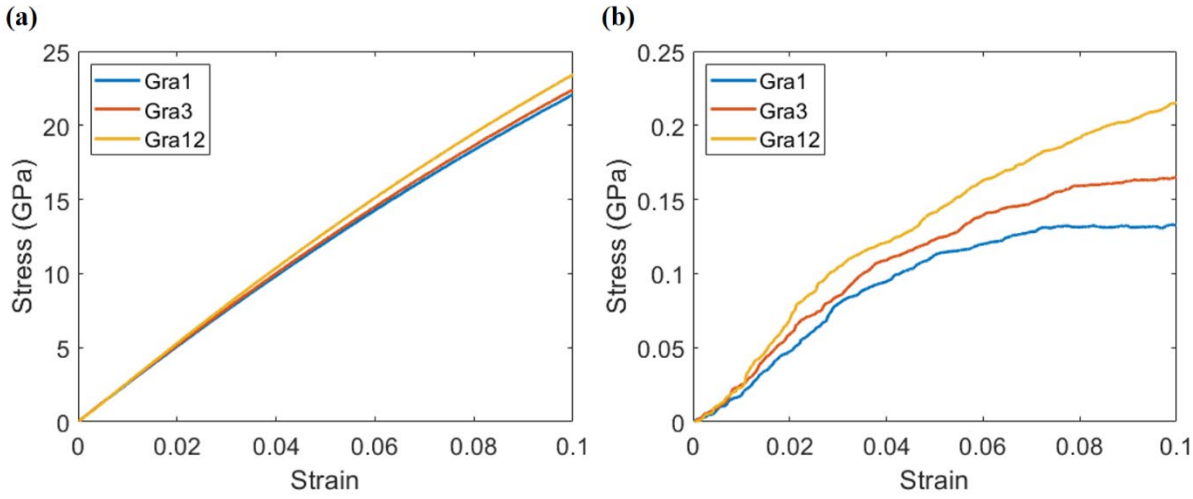

Figure 3.4: (a) The stress-strain relationships of the entire system under uniaxial tensile deformation, where the elastic responses of the films show slight differences. (b) The stress-strain relationship of the polymer phase and thinner polymer phases (larger n) show stiffer and stronger behavior.

The nanoconfinement effects dependent on nanostructures can also be observed from the free vibration frequency results of the films. The obtained frequency value is positively related to Young's modulus of the film. This trend resembles the relationship between the resonance frequency f and the elastic modulus E on a continuum beam predicted theoretically [88, 89]

$$f = \sqrt{EI/Al^3} \tag{3.1}$$

where I is the second moment of area, A is the cross-sectional area, and l is the effective length of the system. For all the investigated systems in this study, they have the same length l and similar moment of inertia I and cross-sectional area A. In addition, the system is periodic and uniform in the width direction (y-direction) and thus can be simplified as a 2D beam system. Equation (3.1) shows that f positively depends on E, with a power of 0.5.

This aligns with my result (see Table 3.1), in which the power value is fitted as ~0.57. The deviation might be due to the slight difference in thickness of the system after equilibration processes and the different densities of the graphene and PMMA phases. Nevertheless, the increasing trend of both f and E with increasing n clearly demonstrates the nanoconfinement effect within the nanocomposites. This result shows that the internal nanostructures can tune the in-plane stiffness of layered nanocomposite films; it also indicates that the in-plane stiffness of films can be explored and compared through vibrational analysis.

Table 3.1: The mean value and standard deviation (S.D) of Young's modulus (E) and free vibration frequencies (f) of different films.

Film	E (GPa)	f (GHz)
Gra(n)	Mean (S.D.)	Mean (S.D.)
1	246.9 (1.8)	4.55 (0.07)
2	248.0 (1.8)	4.61 (0.08)
3	252.0 (1.8)	4.75 (0.08)
4	252.2 (2.1)	4.76 (0.04)
6	255.8 (2.3)	4.86 (0.07)
8	257.8 (2.1)	4.87 (0.04)
12	260.8 (1.5)	5.03 (0.06)

3.3.2 Influence of projectile shape on ballistic impact behavior

The responses of investigated nanostructured films under high-velocity impact from either sharp-nosed or blunt-nosed projectiles are compared in this section. Simulation results find that except for the Gra1 case, which has no repetitive features, the responses for other cases are similar under the impact of the two types of projectiles. For the Gra1 case, the major difference between the two cases is in the failure mechanisms of the top and bottom faces. The difference is attributed to the different stress concentrations upon impact and the shape of stress waves propagating through the thickness direction.

Figure 3.5 shows the dynamic failure of the Gra1 system upon impact from both blunt-nosed and sharp-nosed projectiles with the same impact velocity. At this point, both projectiles rebound and show similar residual velocity after impacting the film. Localized failure in the top layers of both systems is observed upon impact due to the immense stress localized on the strike-face. Relatively more fragments can be observed in the sharp-nosed projectile system as the resulted localized stress in the top graphene sheets is higher than the case in the blunt-nosed projectile system (see Figure 3.5).

Even though the projectile rebounded, a compressive stress wave keeps propagating downward for both cases. Patterns that are similar to crazing-like deformations can be observed within the PMMA layer in both cases. Such deformation mechanisms will be discussed in detail in Section 3.3.4. Interestingly, it is found that under the blunt-nosed projectile impact, the bottom bilayer graphene cap is destroyed by the stress wave, despite that not all graphene sheets at the strike side are fractured. This behavior is similar to the

previous study illustrating the spalling-like failure of MLG under blunt-nosed projectile impact [69], where cracks can localize in the bottom section of MLG. The study has shown that this type of failure is due to the reflection of the planar shape of the compressive stress wave into a tensile wave. In addition, the planar stress wave experiences limited attenuation during propagation, although the interfaces between graphene and PMMA will lead to a certain level of stress wave dissipation. Such dissipation at interfaces is also reflected in the fact that the spalling-like failure does not show up in nanostructures with a higher number of repetitions.

In contrast, under the impact of the sharp-nosed projectile, the bottom bilayer graphene sheets do not show failure. The sharp-nosed projectile system forms an expanding wave originated from the impact site. The wave propagates with a sphere-shaped wavefront, as illustrated in our previous continuum-level simulations showing the wave shape [69]. This leads to faster attenuation of the compressive waves. The more significant extent of fragmentation at the top surface further lowers the intensity of the compressive wave. As a result, the bottom bilayer graphene cap remains intact.

In addition, the same pattern is not observed in cases where the projectile first impacts the PMMA side as the PMMA phase on the strike side constantly dissipates the kinetic energy of the projectile, leaving a much weaker compressive wave which is insufficient to lead to spalling-like failure. It indicates that the prerequisites for spalling-like failure are a stiff and less-dissipative medium at the strike side to generate a strong compressive wave and a planar shape wavefront.

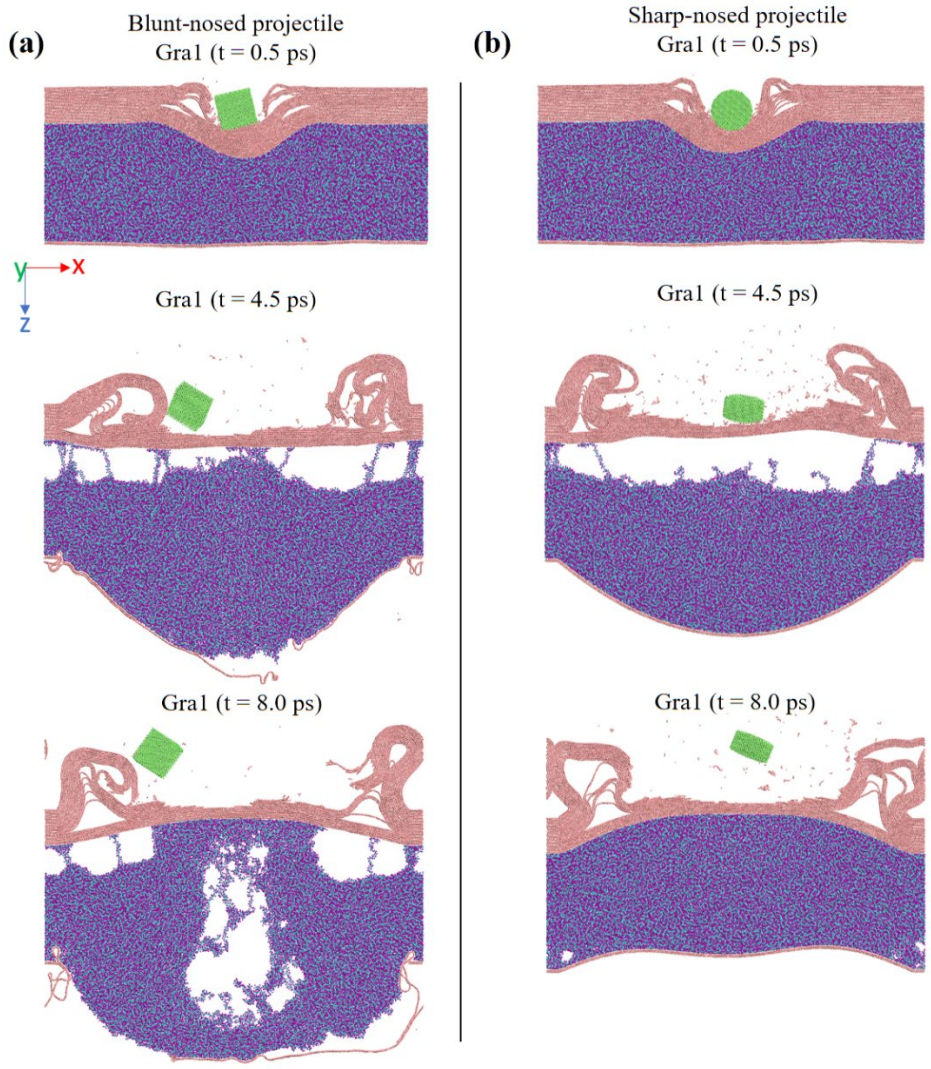

Figure 3.5: The different failure mechanisms in the Gra1 system for (a) blunt-nosed and (b) sharp-nosed projectile with V_0=4000 *m/s* at different time frames. The graphene cap layers at the bottom are fractured under the impact of the blunt-nosed projectile but not in the sharp-nosed projectile case.

Despite the different failure mechanisms observed at the bottom graphene cap layers, results find that the cap layer breakage does not affect the impact resistance, i.e., the V_{50} of the investigated films. This is because graphene cap layers contribute minimally

to the total ballistic performance of the system, which will be discussed in section 3.3.3. It is also worth noting that the different failure mechanisms at the bottom graphene cap layers only occur in a narrow velocity window. The Gra1 film shows similar responses under both projectiles at other V_0. In Figure 3.6 - 3.8, a similar deformation pattern can be observed for the Gra1 film when impacted by a blunt-nosed or sharp-nosed projectile at different V_0, in contrast to the discussed observation of the different deformation patterns between blunt-nosed or sharp-nosed projectile at $V_0 = 4000$ *m/s*, which is shown in Figure 3.5 in the above paragraphs.

When V_0 is relatively small (i.e., 3800 *m/s*), the graphene cap layers do not fracture in either case, as shown in Figure 3.6. At $V_0 = 4200$ *m/s*, both projectiles lead to the fracture of the graphene cap layers without totally penetrating the top thick graphene layers (Figure 3.7), and when V_0 increases to 4500 *m/s*, both the blunt-nosed and sharp-nosed projectiles can penetrate the film, as shown in Figure 3.8. These simulation results show that the different failure mechanisms at the bottom graphene cap layers only occur in a narrow velocity window, indicating the different shape of projectiles has a limited and non-decisive influence when evaluating the overall impact resistance of the systems.

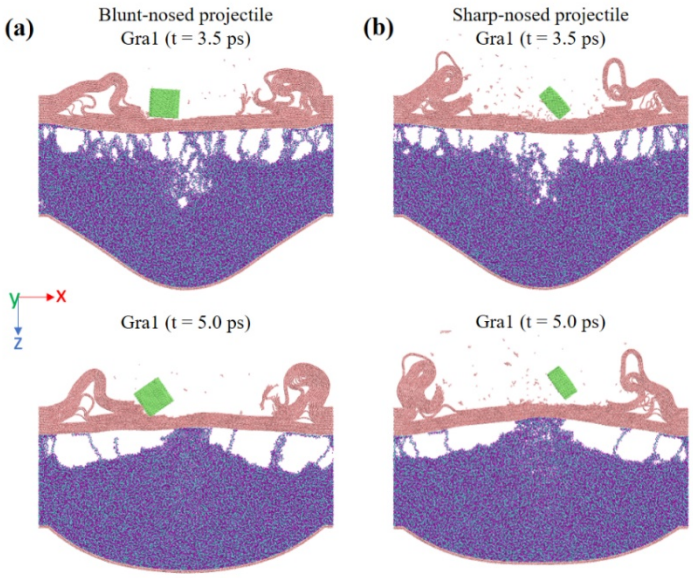

Figure 3.6: The different failure mechanisms on the Gra1 system for (a) blunt-nosed and (b) sharp-nosed projectile with $V_0 = 3800$ *m/s*. All the snapshots are shown using the same coordinate axis on the middle left.

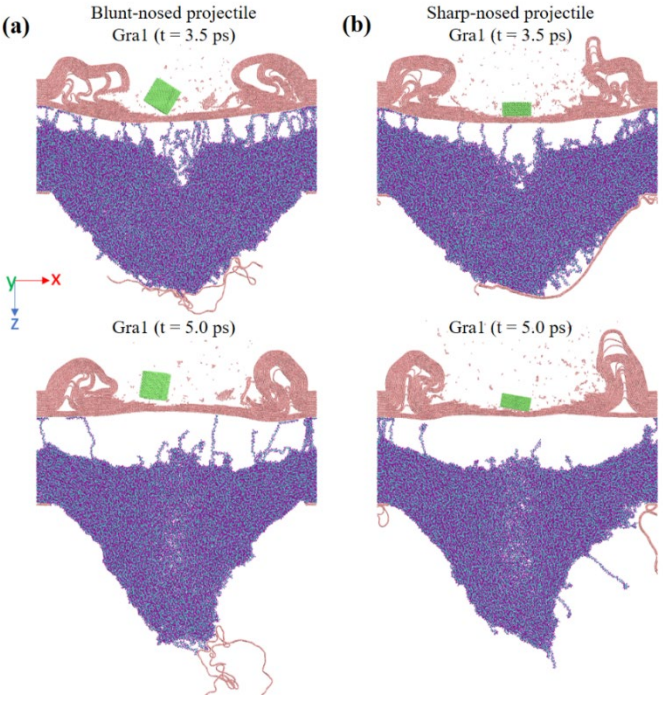

Figure 3.7: The dynamic responses of the Gra1 system under the impact of (a) blunt-nosed and (b) sharp-nosed projectile with $V_0 = 4200$ *m/s*.

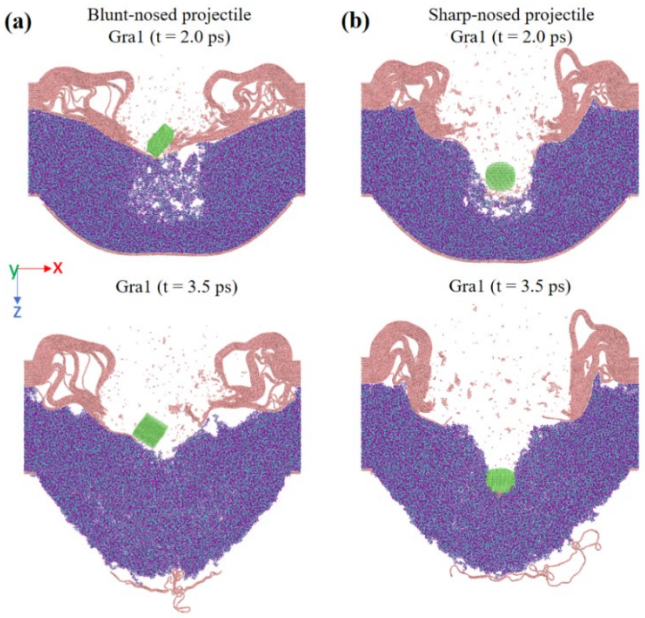

Figure 3.8: The different failure mechanisms on the Gra1 system for (a) blunt-nosed and (b) sharp-nosed projectile with $V_0 = 4500$ *m/s*.

Furthermore, more comparisons of blunt-nosed projectile vs. sharp-nosed projectile impact for Gra2 (Figure 3.9) and Gra3 (Figure 3.10) cases are included in this section, which also shows consistent responses. Figure 3.9 and 3.10 illustrate the similarity in the deformation patterns of Gra2 and Gra3 films under the impact of the two projectiles, respectively. Crazing-like deformation appears in the bottom confined PMMA layer, where large voids and interfacial detachment dissipate a significant portion of impact energy. However, the spalling-like failure is no longer observed in these two systems. This is likely due to the internal graphene layers serve as barricades as the compressive wave propagates downward, obstructing and reflecting such wave energy so that the remaining portion of such energy eventually reaches the bottom is not sufficient to break the capped graphene

sheets. As the systems become more confined, the obstruction from the interlayer transfer occurs much more frequently; as a result, the influence of projectile shape only appears within a small V_0 range in the Gra1 case.

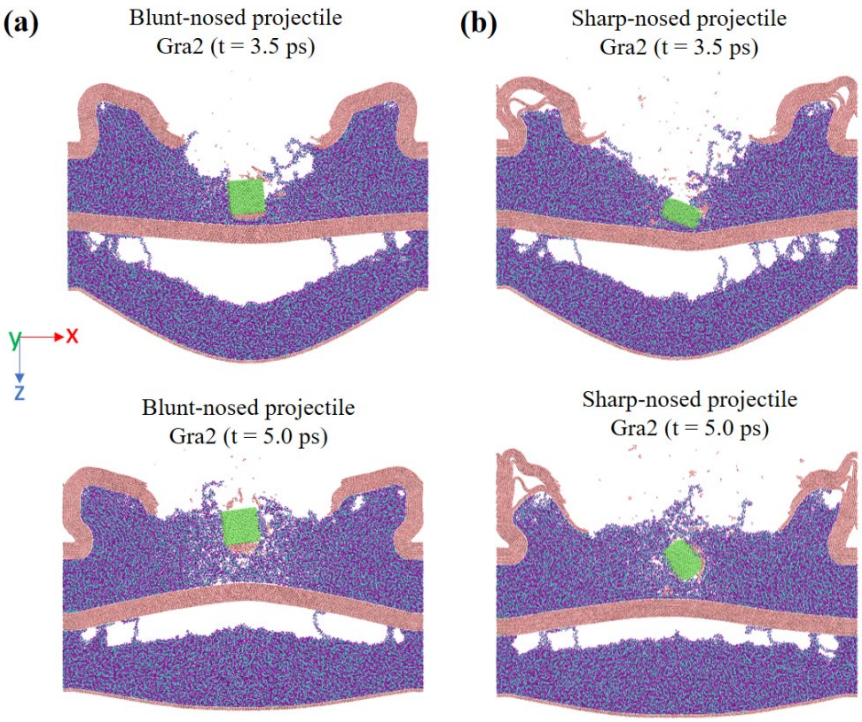

Figure 3.9: The different failure mechanisms on the Gra2 system for (a) blunt-nosed and (b) sharp-nosed projectile with $V_0 = 4000$ *m/s*.

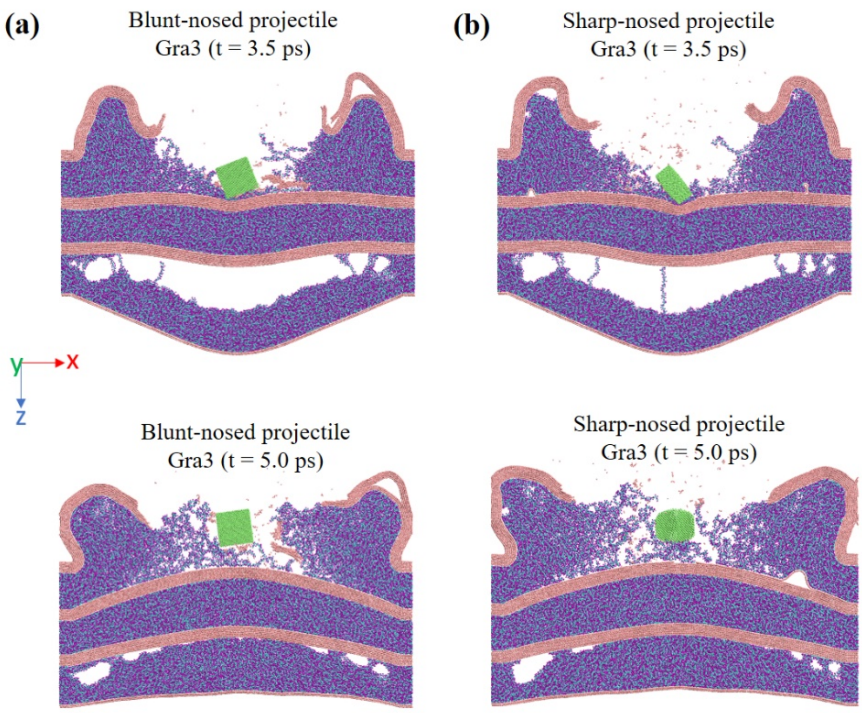

Figure 3.10: The different failure mechanisms on the Gra3 system for (a) blunt-nosed and (b) sharp-nosed projectile with $V_0 = 4000$ *m/s*.

Note that the projectile can rotate during the penetration process. This rotation is highly dynamic and depends on the internal nanostructures, as shown in Figure 3.11. To ensure the initial configurations of the system do not influence the results obtained in this study, my study has conducted simulations on each system (Gra1 to Gra12) using multiple structure data files. The additional simulations also enable us to check the potential effect of projectile rotation on the penetration process and the overall evaluation of the impact resistance. Since the confined PMMA layer in the system is generated using a random walk method that results in a different amorphous inner structure upon each generation [61], each data file for the same film has small configurational differences within the PMMA

layers after the equilibrium process. The structural differences also lead to slightly different rotating behaviors of the projectile during the perforation process. Figure 3.11 shows the different trials of the PMMA1 system. Similar V_{50} is obtained for the three films as well as other investigated films with different trials, thus confirming that the rotation of the projectile does not affect my evaluation of the impact resistance of different films.

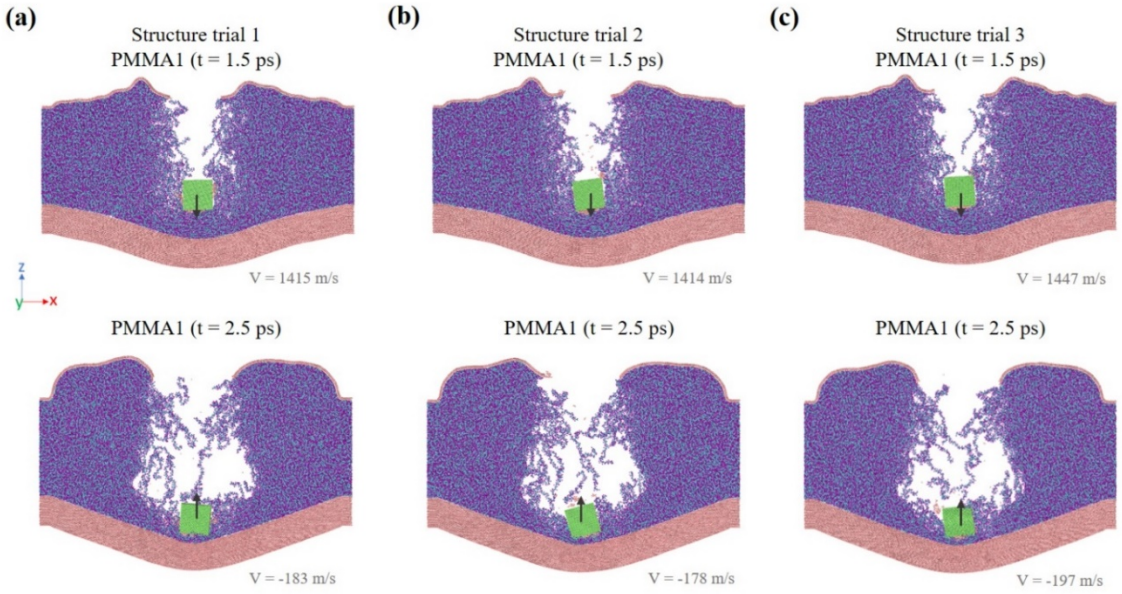

Figure 3.11: The penetration process of the blunt-nosed projectile is independent of its rotation behaviors upon impacting the PMMA1 system with V_0 = 4000 *m/s*, as shown in different trials.

3.3.3 Influence of the strike face on the impact responses of asymmetric films

Comparison of dynamic mechanical behaviors during the ballistic impact of pure graphene, Gra1, and PMMA1 are shown in Figure 3.12. These snapshots correspond to

impact by a blunt-nosed projectile with a V_0 of 4000 *m/s*. Previous section (Section 3.3.2) has discussed the spalling-like failure in the Gra1 system. The simulations on pure graphene (i.e., 26 graphene sheets) also show the stress-induced failure mechanisms at the bottom section, similar to the previous study [69]. During the simulations, it is also observed that some of the graphene sheets fracture at both ends, where strictly clamped boundary conditions are enforced. These localized failures are due to the stress concentrations resulted from in-plane propagated waves. From previous studies, it is shown that the targeted film size needs to be large enough to eliminate the in-plane wave-induced failure [69]. The choice of the width of the systems in this study is limited by computational resources; thus, resulted in the in-plane waves. Further note that the finite size MLG used in this study would lead to the deteriorated impact resistance of MLG. However, when comparing the dynamic failure of pure graphene and nanocomposite systems, as in Figure 3.12(a) and (b), results indicate that by adding a dissipative soft polymer phase, the deterioration from finite in-plane size is greatly alleviated. This highlights the role of the soft phases in nacre-inspired nanocomposites in resisting impact.

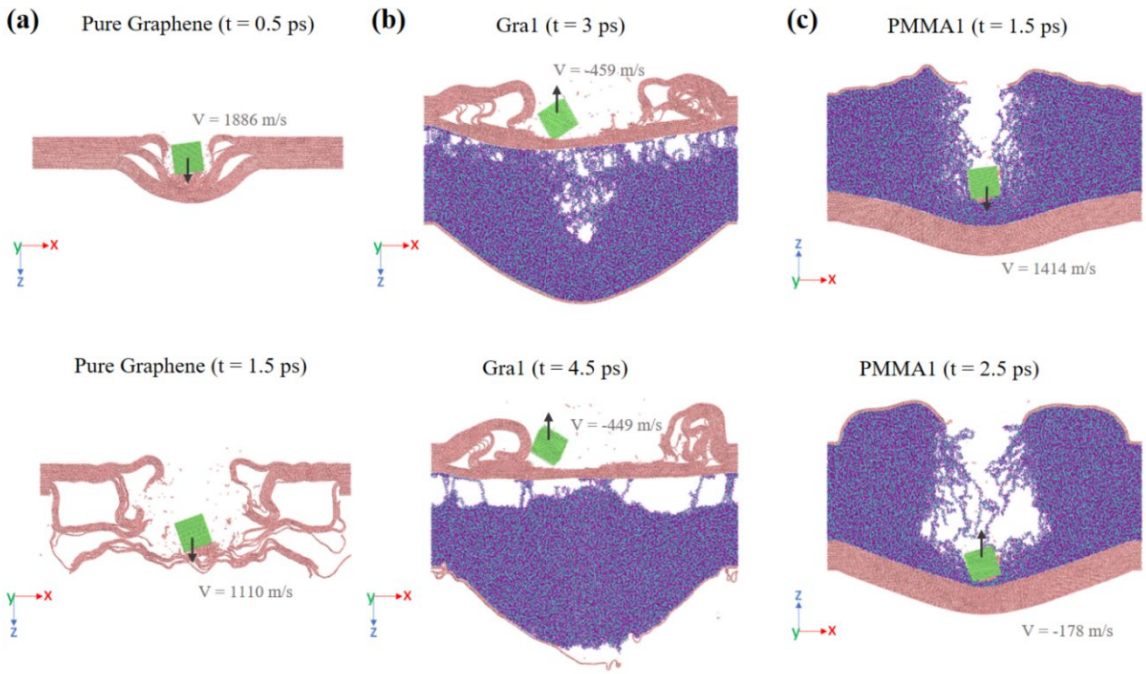

Figure 3.12: The trajectories of (a) pure graphene structure with 26 layers of graphene sheets, (b) Gra1 structure, and (c) PMMA1 structure under the impact of the blunt-nosed projectile with $V_0 = 4000$ *m/s*. The arrow on the projectile indicates its moving direction.

This paragraph then compares the different behaviors of PMMA1 and Gra1. When the projectile impacts the bulk MLG phase first for the Gra1 case, the polymer phase does not significantly contribute to the absorption of kinetic energy. Figure 3.12(b) shows that the projectile bounces off from the strike-face before voids within the PMMA phases are observed. A major portion of the kinetic energy from the projectile is absorbed by the strike-face, graphene sheets, which resulted in bond breakages and delamination of the top graphene surface. The thick PMMA film, however, transfers a small portion of the energy from the shock wave induced by the strike to the bottom of the structure and creates a spalling effect. The effect occurs much later than the initial strike since the compressive

wave speed slows down in the polymer phase. Conversely, when the PMMA film is on the strike-face, the polymer phase provides natural resistance to the projectile, of which the kinetic energy significantly dissipates as it penetrates through the polymer film (Figure 3.12(c)). When impacting on the PMMA side, under the same V_0, the graphene sheets underneath PMMA1 stay intact, and the films show a much better impact resistance compared to the Gra1 case. This observation agrees with recent studies that the viscoelastic deformation of the PMMA film contributes greatly to dissipating the energy when positioned as the strike-face [41, 60, 90, 91].

The results obtained from the simulations provide valuable insights into the design strategy of protective thin films. When designing a protective nanostructured film using alternating soft and hard phases, a more confined structure leveraging the nanoconfinement effect from the hard phase to the soft phase should be considered if the design target is higher in-plane stiffness. Adding a viscoelastic phase (i.e., polymeric thin film) on top of stiff plates can significantly improve the impact resistance. This design strategy can have great potential as it does not require any disassembly procedure yet still achieves a significant enhancement on ballistic impact resistance.

3.3.4 Effect of nanostructures on impact resistance and deformation mechanisms

This section looks into the effect of nanostructures on the impact resistance of the studied MLG-PMMA films and the associated deformation mechanisms.

To quantitatively compare the impact resistance of films with different nanostructures, V_{50} are measured and analyzed first. V_{50} is usually referred to as the lowest velocity that fully penetrates the target with a 50% possibility. The variation in residual velocity (V_r) of the projectile versus the impact velocity (V_0) is shown (see Figure 3.13). The V_r is captured as the approximate constant velocity of the projectile after the perforation process. A positive value indicates a full penetration during the test, whereas a negative one indicates the projectile rebounded from the film. In this computational study, the V_{50} is approximated as the V_0 value corresponding to zero V_r, which can be numerically determined by the cross point between $V_r = 0$ line and the linear interpolation between two consecutive data points. These results show that the V_{50} of the films is independent of the shape of the projectiles.

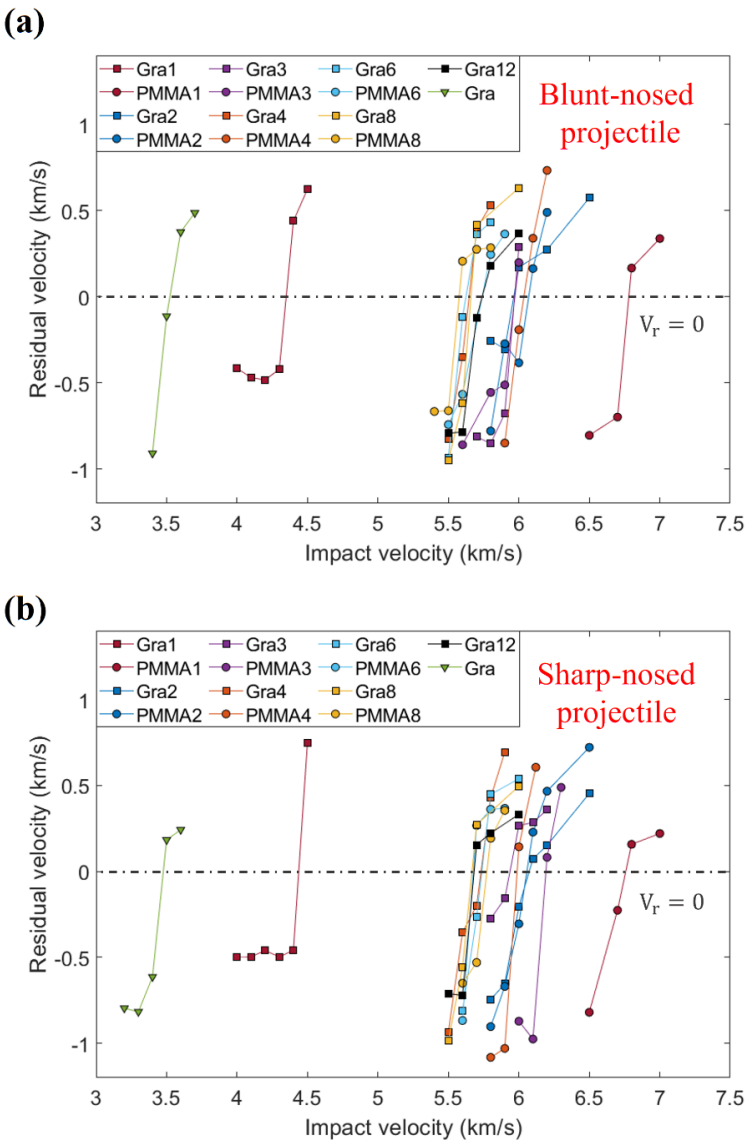

Figure 3.13: Residual velocity (V_r) vs. initial velocity (V_0) of the (a) blunt-nosed projectile and (b) sharp-nosed projectile impacting different films.

All the nanocomposite films show an improvement on V_{50} comparing to the pure graphene sheets in Figure 3.13. The simulation results indicate that positioning a thick polymer film on top of the stiff MLG phase as the strike face (as in the case of PMMA1)

leads to the most significant improvement in ballistic resistance. The PMMA1 has the highest V_{50} among all films and is roughly 50% higher comparing to that of Gra1. As illustrated in the previous section, the PMMA film at the strike-face significantly dissipated the impact energy, which allows the graphene sheets underneath to stay intact. The Gra1 exhibits the lowest V_{50} among all the investigated nanocomposite films, as the viscoelastic behavior of the PMMA film does not contribute to the resistance provided by the graphene sheets on the strike-face, at least in the nanocomposite films studied herein (see Figure 3.11(b)). For Gra8 and Gra12, however, they do not show a significant difference with projectile impacting on different sides. This is because the effects of strike-face and finite sizes become diminished for these structures as they become more symmetric, and the films exhibit gradual and sequential failure during the perforation.

Even though my study indicates that using two single bulk PMMA and MLG phases while making the PMMA film on top achieves the highest V_{50} Such design leads to unbalanced structures and a tradeoff from decreasing in-plane performance, as shown in Section 3.3.1. In addition, limited by the system size, higher repetitions only result in very thin PMMA phases. As a result, only the PMMA1 case shows the obvious 'dragging' effect of the polymer phase. If the total thickness increases to micro-sizes, the polymer phases for higher repetition structures may also play a considerable role in dissipating energy. Combined with other deformation mechanisms (to be discussed next) and direct nanoconfinement effect, higher repetitions might perform better under impact when the film thickness reaches micron sizes. It is worth noting that the projectile impact simulations

only generate insights into the localized impact failures, while the large-area impact, such as blast, can be better studied using other types of simulations [92, 93].

Finally, this paragraph discusses the deformation mechanisms in layered nanocomposites that potentially contribute to energy dissipation/absorption capability under impact loading conditions. The result simulation trajectories reveal interesting deformation mechanisms within the nanostructured films after a projectile impacted them with low to medium velocity. In those cases, the strike-face stays intact or experiences minimal crack or failure. These cases are the predominant loading scenarios of various biomaterials during the life period of the living organisms. In addition to designing protective applications perspective, those cases are also likely to be the ideal cases for protection barriers under impact loading as the induced failure is contained within the structure while having the surface of it unharmed or less harmed by external objects.

As shown in Figure 3.14, unique crazing-like deformations are observed in the soft PMMA phases after the impact of the sharp-nosed projectile. We note that the deformation mechanisms are very similar using the blunt-nosed projectile. After the projectile impacts on the strike-face, a compressive wave forms and propagates downwardly. Due to the relatively slow wave propagation speed and wave reflections at the polymer/graphene interface, heterogeneous deformation arises in the thickness direction of the films. Specifically, when the compressive wave propagates downwardly, the upper layers become relaxed first and vibrate upwardly and towards the projectile direction, while the bottom part of the film is still deformed downwardly due to the influence from the compressive wave. This effect induces tensile stress to certain confined PMMA phases, which lead to

microvoid formations. The microvoids expand in the x-direction that is normal to the stress wave, and they eventually develop into crazing-like deformation zones [94-96]. The impact energy from the projectile is effectively dissipated during the development of the crazes, which involves significant interchain sliding within the PMMA phase. Through this source of energy dissipation, the vibration of the films is significantly damped. Similar deformation can be observed on all investigated films with the layered nanostructure (see Figure 3.14). The crazing-like deformation in the PMMA phases is separated by the stiff graphene sheets and happens in multiple PMMA phases. The stiff graphene sheets maintain the integrity of the whole film and prevent it from falling apart. The utilized CG simulation models also show good adhesion between graphene and PMMA, which prevents the interfaces from complete delamination.

To summarize the key deformation mechanisms, the viscoplastic behavior of the PMMA films dissipates a significant portion of energy, which is further enhanced by the crazing-like deformation developed in multiple layers of PMMA, while the stiff graphene sheets provide overall robustness of the structure and avoid total failure of the film. It is expected that these observed deformation mechanisms would improve the energy dissipation capability of layered nanostructures in protective applications.

Noted that such crazing-like deformation is not observed when the film is under a higher velocity impact (i.e., V_0 larger than 4500 *m/s*). When under such high strain loading, the projectile can start penetrating the film before the crazing-like deformation within the PMMA phase occurs. The perforation process significantly dissipates the impact energy,

hindering the global vibration of the nanocomposite films. It also breaks the integrity of the PMMA phases, which limits the formation of the microvoids.

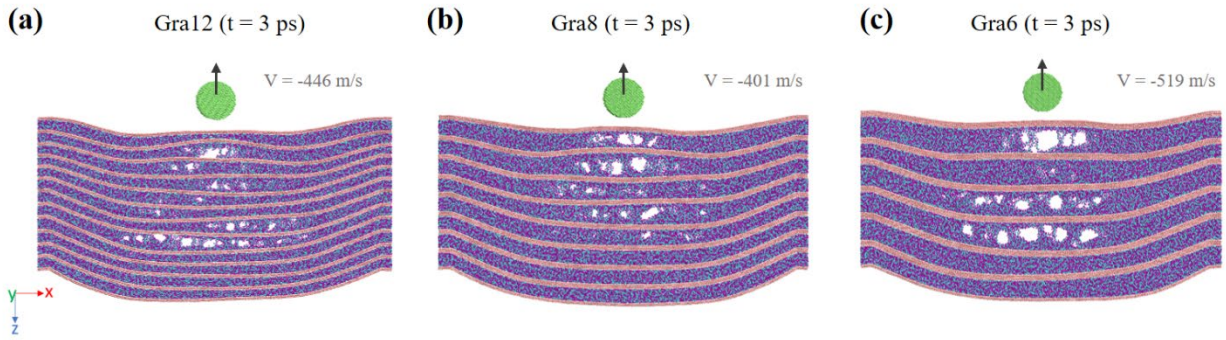

Figure 3.14: Crazing-like deformation in nanolayered films of (a) Gra12, (b) Gra8, and (c) Gra6 under low- to medium-velocity impact from the sharp-nosed projectile with $V_0 = 2000$ *m/s*.

3.4 Conclusion

This chapter presented work of conducting CG-MD simulations on nacre-inspired MLG-PMMA nanocomposite films and investigated their mechanical properties and dynamic failure mechanisms. The effect of nanostructure and layer thickness on elastic modulus, impact resistance, and deformation mechanisms are mainly focused on and discussed.

My study finds that films with a more confined structure (i.e., decreasing layer thickness and higher number of repetitions) yield higher elastic modulus through uniaxial stretching and out-of-plane free vibration simulations. The enhancement is attributed to the

nanoconfinement effect on the nanoscale thin PMMA films from adjacent stiff graphene sheets.

Ballistic impact simulation is then conducted to study the dynamic failure mechanisms and the impact resistance of different nanostructured films, indicated by the V_{50} value. It is observed that although the V_{50} of the investigated films impacted by sharp-nosed or blunt-nosed projectiles are very much identical; the blunt-nosed projectile can lead to an early spalling-like failure at the bottom surface of a single repetition structure. When the repetition number increases, the films fail by sequential penetration instead. Interestingly, for single repetition film, I also observe that the V_{50} differs significantly depending on the strike-face. By placing the PMMA phase on the top of the MLG, the viscoelastic behavior of the PMMA drastically drags the projectile during penetration, resulting in higher V_{50}. In contrast, by placing the PMMA film under the MLG phase, MLG experiences direct impact from the projectile instead. The influence of the stress waves and finite boundary condition leads to a much lower V_{50} eventually. Further study on the deformation mechanisms of layered nanocomposite films under the low-velocity impact is made. The nacre-inspired layered nanocomposites develop crazing-like deformation within the polymer phases under smaller velocity impact load, significantly dissipating the impact energy. This deformation mechanism can be potentially leveraged in the future design of nanostructured protective films.

Chapter 4 Summary and Outlook

4.1 Summary

In this thesis, CG-MD simulations have been performed on the nacre-inspired MLG-PMMA nanocomposites. The simulations have been designed to investigate the ballistic performance of the material under impact based on altering its internal structure arrangement. A brief overview and the background of MD simulations and the corresponding CG model of the investigated system have been discussed (Chapter 2). The behavior of this nanocomposite material in representative problems, i.e., tensile test, nanoindentation, and high-velocity impact simulations, are simulated and studied (Chapter 3). The results obtained from these problems have been systematically compared and analyzed. The key features and findings for the main chapter (Chapter 3) are summarized as follows:

The study investigates the impact resistance of the MLG-PMMA layered nanocomposites. By altering the internal structure arrangement, the elastic modulus and stiffness can be tuned. The nanoconfinement effect contributed from the polymer phases resulting in the enhancement of stiffness with a more confined system. It is also found that different structure arrangements can have a huge influence on the ballistic performance, particularly the position of the PMMA layer. The position of the polymer layer largely affects how the kinetic energy from the projectile is transferred and absorbed, in which results show that placing the polymer block at the strike-face leads to a better impact

resistance of the overall system due to its viscoelastic behavior that dissipates the energy effectively. Furthermore, confined systems exhibit gradual failure and are showing the capability to contain crazing-like deformations under lower velocity impact during the perforation process. In conclusion, this chapter illustrates that the internal nanostructure of the nacre-inspired, layered MLG-PMMA nanocomposite films plays a significant role in the mechanical properties and dynamic failure mechanisms. More importantly, the observations and results from this work provide important insights into potential design strategies of protective thin films.

4.2 Future work

There are multiple aspects that can be explored in future work. First, the current work is conducted based on the objective to understand the dynamic mechanisms of the layered nanocomposites that can better contain or dissipate incoming impact energy. It would be interesting to compare the investigated material (i.e., MLG-PMMA nanocomposites) with other types of nacre-inspired nanocomposites structure that also consists of layers of stiff and soft phases. An immediate step will be to alter the current configuration or loading condition of the system to make it consistent with other work in this research area so that quantifiable impact resistance such as V_{50} can be compared with other data on the same basis.

Second, since the current work adopted a ballistic impact approach to study the ballistic performance of the structure, localized failure of delamination on the strike surface is inevitable. It is important to understand the underlying kinetic energy absorption

mechanisms towards the perspective to tailor the impact resistance of such nanolayered structure. One potential approach will be to conduct the impact test simulations using "planar impact", in which a flat slab can be adhered to the strike-face and generate shock impact. Since the slab is attached to the structure itself, localize failure can be largely eliminated, allowing the kinetic energy to transfer directly to the overall system.

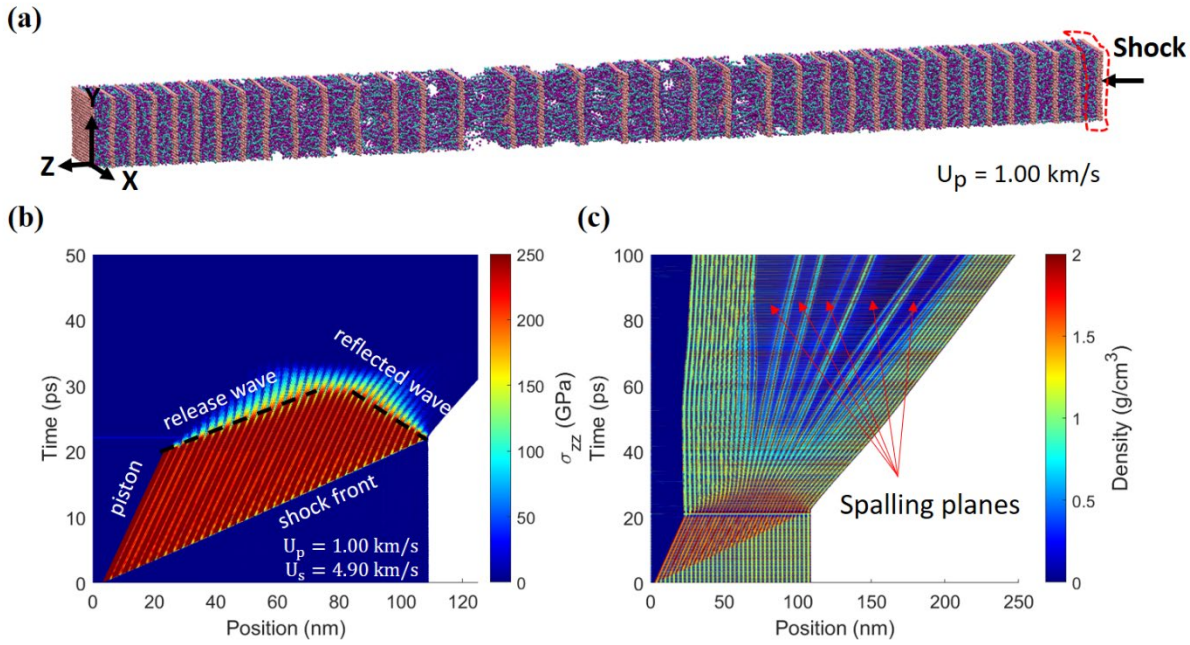

Figure 4.1: Simulation setup of a planar impact simulation on Gra36 structure. (a) Basic schematic of the planar impact simulation, in which the portion of the structure circled in red is defined as a slab and initiated with a velocity of $U_p = 1\ km/s$. (b) The surface plot of the stress σ_{zz}; (c) The surface plot of the density along the direction of wave propagation.

Figure 4.1 shows the results that can be obtained using a planar impact simulation on the Gra36 system. Gra36 system follows the same terminology method, in which 36 repetition modules are stacked together and capped with bilayer graphene sheets at the end.

This forms a system with 6 *nm* * 6 *nm* * 108 *nm* at x-, y-, and z-direction, respectively, allowing a sufficient distance at the longitudinal direction (i.e., z-direction) for the shock wave to propagate. With the entire portion of the kinetic energy transferring through the structure, the results are able to show the wave propagation clearly with little noise (see Figure 4.1(b)). The density of the system at each point can also provide meaningful information since the interferences from external objects or constraints are none or limited (see Figure 4.1(c)). Moreover, it might be possible to quantify the impact resistance of the system using these simulation results. It will be interesting to explore the approach to better quantitively compare the impact resistance of the material, which will be a critical requirement for illustrating the performance when designing protective applications.

Lastly, the investigated system considered the stiff phase as a continuous graphene nanosheet within each layer, whereas the real nacre shells are typically discretized fibers in their stiff phases. To approach the real energy dissipation mechanism on nacre shell under impact loads, it is necessary to design a better system configuration that has higher fidelity towards a genuine bio-structure. The research outcomes of addressing this challenge would also help enhance the model fidelity of the CG-MD simulations conducted in this work.

Bibliography

1. Grimaldi, A., et al., *Parametric study of a SPH high velocity impact analysis–a birdstrike windshield application.* Composite Structures, 2013. **96**: p. 616-630.
2. Dar, U.A. and W. Zhang, *Polymer based aerospace structures under high velocity impact applications; experimental, constitutive and finite element analysis.* Journal of Mechanical Science and Technology, 2015. **29**(10): p. 4259-4265.
3. Grossman, E., I. Gouzman, and R. Verker, *Debris/micrometeoroid impacts and synergistic effects on spacecraft materials.* MRS bulletin, 2010. **35**(1): p. 41-47.
4. Anagnostopoulos, G., et al., *Mechanical stability of flexible graphene-based displays.* ACS applied materials & interfaces, 2016. **8**(34): p. 22605-22614.
5. Winterhalter, C.A., et al., *Development of electronic textiles to support networks, communications, and medical applications in future US Military protective clothing systems.* IEEE Transactions on Information Technology in Biomedicine, 2005. **9**(3): p. 402-406.
6. Zhang, X. and H. Hao, *The response of glass window systems to blast loadings: An overview.* International Journal of Protective Structures, 2016. **7**(1): p. 123-154.
7. Chen, S., et al., *Numerical analysis of impact failure of automotive laminated glass: a review.* Composites Part B: Engineering, 2017. **122**: p. 47-60.
8. Imbalzano, G., et al., *Blast resistance of auxetic and honeycomb sandwich panels: Comparisons and parametric designs.* Composite Structures, 2018. **183**: p. 242-261.
9. Crawford, D.M. and J.A. Escarsega, *Dynamic mechanical analysis of novel polyurethane coating for military applications.* Thermochimica acta, 2000. **357**: p. 161-168.
10. Villanueva, G.R. and W. Cantwell, *The high velocity impact response of composite and FML-reinforced sandwich structures.* Composites Science and Technology, 2004. **64**(1): p. 35-54.
11. Ramadhan, A., et al., *High velocity impact response of Kevlar-29/epoxy and 6061-T6 aluminum laminated panels.* Materials & Design, 2013. **43**: p. 307-321.
12. Dudek, K.K., et al., *Impact resistance of composite magnetic metamaterials.* Scientific reports, 2019. **9**(1): p. 1-9.
13. Cheeseman, B.A. and T.A. Bogetti, *Ballistic impact into fabric and compliant composite laminates.* Composite structures, 2003. **61**(1-2): p. 161-173.
14. Lee, J.-H., et al., *High strain rate deformation of layered nanocomposites.* Nature communications, 2012. **3**(1): p. 1-9.
15. Roduner, E., *Size matters: why nanomaterials are different.* Chemical Society Reviews, 2006. **35**(7): p. 583-592.
16. Halperin, f.W., *Quantum size effects in metal particles.* Reviews of Modern Physics, 1986. **58**(3): p. 533.
17. Takagi, H., et al., *Quantum size effects on photoluminescence in ultrafine Si particles.* Applied Physics Letters, 1990. **56**(24): p. 2379-2380.

18. Cuenot, S., et al., *Surface tension effect on the mechanical properties of nanomaterials measured by atomic force microscopy.* Physical Review B, 2004. **69**(16): p. 165410.
19. Wang, Y. and N. Herron, *Nanometer-sized semiconductor clusters: materials synthesis, quantum size effects, and photophysical properties.* The Journal of Physical Chemistry, 1991. **95**(2): p. 525-532.
20. Yoffe, A.D., *Low-dimensional systems: quantum size effects and electronic properties of semiconductor microcrystallites (zero-dimensional systems) and some quasi-two-dimensional systems.* Advances in Physics, 1993. **42**(2): p. 173-262.
21. Kayanuma, Y., *Quantum-size effects of interacting electrons and holes in semiconductor microcrystals with spherical shape.* Physical Review B, 1988. **38**(14): p. 9797.
22. Zhang, Q., et al., *Nanomaterials for energy conversion and storage.* Chemical Society Reviews, 2013. **42**(7): p. 3127-3171.
23. Jing, G., et al., *Surface effects on elastic properties of silver nanowires: contact atomic-force microscopy.* Physical review B, 2006. **73**(23): p. 235409.
24. Asaro, R.J., P. Krysl, and B. Kad, *Deformation mechanism transitions in nanoscale fcc metals.* Philosophical Magazine Letters, 2003. **83**(12): p. 733-743.
25. Misra, A., J. Hirth, and H. Kung, *Single-dislocation-based strengthening mechanisms in nanoscale metallic multilayers.* Philosophical Magazine A, 2002. **82**(16): p. 2935-2951.
26. Dong, H., B. Wen, and R. Melnik, *Relative importance of grain boundaries and size effects in thermal conductivity of nanocrystalline materials.* Scientific reports, 2014. **4**(1): p. 1-5.
27. Wagner, M., *Structure and thermodynamic properties of nanocrystalline metals.* Physical Review B, 1992. **45**(2): p. 635.
28. Wang, N., et al., *Effect of grain size on mechanical properties of nanocrystalline materials.* Acta Metallurgica et Materialia, 1995. **43**(2): p. 519-528.
29. Meyers, M.A., A. Mishra, and D.J. Benson, *Mechanical properties of nanocrystalline materials.* Progress in materials science, 2006. **51**(4): p. 427-556.
30. Lee, J.-H., et al., *Dynamic mechanical behavior of multilayer graphene via supersonic projectile penetration.* Science, 2014. **346**(6213): p. 1092-1096.
31. Cai, J. and R. Thevamaran, *Superior Energy Dissipation by Ultrathin Semicrystalline Polymer Films Under Supersonic Microprojectile Impacts.* Nano letters, 2020. **20**(8): p. 5632-5638.
32. Himmelberger, S., et al., *Effects of confinement on microstructure and charge transport in high performance semicrystalline polymer semiconductors.* Advanced Functional Materials, 2013. **23**(16): p. 2091-2098.
33. Alcoutlabi, M. and G.B. McKenna, *Effects of confinement on material behaviour at the nanometre size scale.* Journal of Physics: Condensed Matter, 2005. **17**(15): p. R461.

34. Lee, J.-H., J.Y. Chung, and C.M. Stafford, *Effect of confinement on stiffness and fracture of thin amorphous polymer films.* ACS Macro Letters, 2012. **1**(1): p. 122-126.
35. Shao, C. and S. Keten, *Stiffness enhancement in nacre-inspired nanocomposites due to nanoconfinement.* Scientific reports, 2015. **5**(1): p. 1-12.
36. Stafford, C.M., et al., *Elastic moduli of ultrathin amorphous polymer films.* Macromolecules, 2006. **39**(15): p. 5095-5099.
37. Li, C. and A. Strachan, *Effect of thickness on the thermo-mechanical response of free-standing thermoset nanofilms from molecular dynamics.* Macromolecules, 2011. **44**(23): p. 9448-9454.
38. Böhme, T.R. and J.J. de Pablo, *Evidence for size-dependent mechanical properties from simulations of nanoscopic polymeric structures.* The Journal of chemical physics, 2002. **116**(22): p. 9939-9951.
39. Xia, W. and S. Keten, *Interfacial stiffening of polymer thin films under nanoconfinement.* Extreme Mechanics Letters, 2015. **4**: p. 89-95.
40. Dewapriya, M. and S. Meguid, *Comprehensive molecular dynamics studies of the ballistic resistance of multilayer graphene-polymer composite.* Computational Materials Science, 2019. **170**: p. 109171.
41. Dewapriya, M. and R. Miller, *Superior Dynamic Penetration Resistance of Nanoscale Multilayer Polymer/Metal Films.* Journal of Applied Mechanics, 2020. **87**(12).
42. Wegst, U.G., et al., *Bioinspired structural materials.* Nature materials, 2015. **14**(1): p. 23-36.
43. Li, X., et al., *Nanoscale structural and mechanical characterization of a natural nanocomposite material: the shell of red abalone.* Nano letters, 2004. **4**(4): p. 613-617.
44. Song, F., A. Soh, and Y. Bai, *Structural and mechanical properties of the organic matrix layers of nacre.* Biomaterials, 2003. **24**(20): p. 3623-3631.
45. Yang, R., et al., *AFM identification of beetle exocuticle: Bouligand structure and nanofiber anisotropic elastic properties.* Advanced Functional Materials, 2017. **27**(6): p. 1603993.
46. Nikolov, S., et al., *Revealing the design principles of high-performance biological composites using ab initio and multiscale simulations: the example of lobster cuticle.* Advanced Materials, 2010. **22**(4): p. 519-526.
47. Chen, P.-Y., et al., *Structure and mechanical properties of crab exoskeletons.* Acta biomaterialia, 2008. **4**(3): p. 587-596.
48. Zimmermann, E.A., et al., *Mechanical adaptability of the Bouligand-type structure in natural dermal armour.* Nature communications, 2013. **4**(1): p. 1-7.
49. Yang, W., et al., *Protective role of Arapaima gigas fish scales: structure and mechanical behavior.* Acta biomaterialia, 2014. **10**(8): p. 3599-3614.
50. Weaver, J.C., et al., *The stomatopod dactyl club: a formidable damage-tolerant biological hammer.* Science, 2012. **336**(6086): p. 1275-1280.
51. Qin, X., et al., *Impact resistance of nanocellulose films with bioinspired Bouligand microstructures.* Nanoscale Advances, 2019. **1**(4): p. 1351-1361.

52. Sun, J. and B. Bhushan, *Hierarchical structure and mechanical properties of nacre: a review.* Rsc Advances, 2012. **2**(20): p. 7617-7632.
53. Wang, J., Q. Cheng, and Z. Tang, *Layered nanocomposites inspired by the structure and mechanical properties of nacre.* Chemical Society Reviews, 2012. **41**(3): p. 1111-1129.
54. Zhao, H., Z. Yang, and L. Guo, *Nacre-inspired composites with different macroscopic dimensions: strategies for improved mechanical performance and applications.* NPG Asia Materials, 2018. **10**(4): p. 1-22.
55. Chen, C.-T., et al., *Nacre-inspired design of graphene oxide–polydopamine nanocomposites for enhanced mechanical properties and multi-functionalities.* Nano Futures, 2017. **1**(1): p. 011003.
56. Wan, S., et al., *Nacre-inspired integrated strong and tough reduced graphene oxide–poly (acrylic acid) nanocomposites.* Nanoscale, 2016. **8**(10): p. 5649-5656.
57. Xia, W., et al., *Designing multilayer graphene-based assemblies for enhanced toughness in nacre-inspired nanocomposites.* Molecular Systems Design & Engineering, 2016. **1**(1): p. 40-47.
58. Alian, A., M. Dewapriya, and S. Meguid, *Molecular dynamics study of the reinforcement effect of graphene in multilayered polymer nanocomposites.* Materials & Design, 2017. **124**: p. 47-57.
59. Xia, W., et al., *Understanding the interfacial mechanical response of nanoscale polymer thin films via nanoindentation.* Macromolecules, 2016. **49**(10): p. 3810-3817.
60. Dewapriya, M. and R. Miller, *Energy absorption mechanisms of nanoscopic multilayer structures under ballistic impact loading.* Computational Materials Science, 2021. **195**: p. 110504.
61. Hsu, D.D., et al., *Systematic method for thermomechanically consistent coarse-graining: a universal model for methacrylate-based polymers.* Journal of chemical theory and computation, 2014. **10**(6): p. 2514-2527.
62. Ruiz, L., et al., *A coarse-grained model for the mechanical behavior of multilayer graphene.* Carbon, 2015. **82**: p. 103-115.
63. Wei, X., et al., *Recoverable slippage mechanism in multilayer graphene leads to repeatable energy dissipation.* ACS nano, 2016. **10**(2): p. 1820-1828.
64. Xia, W., et al., *Critical length scales and strain localization govern the mechanical performance of multilayer graphene assemblies.* Nanoscale, 2016. **8**(12): p. 6456-6462.
65. Wang, Y. and Z. Meng, *Mechanical and viscoelastic properties of wrinkled graphene reinforced polymer nanocomposites–Effect of interlayer sliding within graphene sheets.* Carbon, 2021. **177**: p. 128-137.
66. Yang, J., et al., *Understanding the mechanical and viscoelastic properties of graphene reinforced polycarbonate nanocomposites using coarse-grained molecular dynamics simulations.* Computational Materials Science, 2021. **191**: p. 110339.

67. Chiang, C.-C., et al., *Dynamic mechanical behaviors of nacre-inspired graphene-polymer nanocomposites depending on internal nanostructures.* Extreme Mechanics Letters, 2021. **49**: p. 101451.
68. Meng, Z., et al., *Reduced ballistic limit velocity of graphene membranes due to cone wave reflection.* Extreme Mechanics Letters, 2017. **15**: p. 70-77.
69. Meng, Z., et al., *Spalling-Like Failure by Cylindrical Projectiles Deteriorates the Ballistic Performance of Multi-Layer Graphene Plates.* Carbon, 2018. **126**: p. 611-619.
70. Meng, Z. and S. Keten, *Unraveling the Effect of Material Properties and Geometrical Factors on Ballistic Penetration Energy of Nanoscale Thin Films.* Journal of Applied Mechanics, 2018. **85**(12).
71. Metropolis, N., et al., *Equation of state calculations by fast computing machines.* The journal of chemical physics, 1953. **21**(6): p. 1087-1092.
72. Alder, B.J. and T.E. Wainwright, *Phase transition for a hard sphere system.* The Journal of chemical physics, 1957. **27**(5): p. 1208-1209.
73. Stuart, S.J., A.B. Tutein, and J.A. Harrison, *A reactive potential for hydrocarbons with intermolecular interactions.* The Journal of chemical physics, 2000. **112**(14): p. 6472-6486.
74. Chenoweth, K., A.C. Van Duin, and W.A. Goddard, *ReaxFF reactive force field for molecular dynamics simulations of hydrocarbon oxidation.* The Journal of Physical Chemistry A, 2008. **112**(5): p. 1040-1053.
75. Tersoff, J., *Empirical interatomic potential for silicon with improved elastic properties.* Physical Review B, 1988. **38**(14): p. 9902.
76. Tersoff, J., *New empirical approach for the structure and energy of covalent systems.* Physical review B, 1988. **37**(12): p. 6991.
77. Verlet, L., *Computer" experiments" on classical fluids. I. Thermodynamical properties of Lennard-Jones molecules.* Physical review, 1967. **159**(1): p. 98.
78. Li, Y., et al., *Challenges in multiscale modeling of polymer dynamics.* Polymers, 2013. **5**(2): p. 751-832.
79. Titov, A.V., P. Král, and R. Pearson, *Sandwiched graphene− membrane superstructures.* ACS nano, 2010. **4**(1): p. 229-234.
80. Marrink, S.J., et al., *The MARTINI force field: coarse grained model for biomolecular simulations.* The journal of physical chemistry B, 2007. **111**(27): p. 7812-7824.
81. Marrink, S.J., A.H. De Vries, and A.E. Mark, *Coarse grained model for semiquantitative lipid simulations.* The Journal of Physical Chemistry B, 2004. **108**(2): p. 750-760.
82. Cranford, S., D. Sen, and M.J. Buehler, *Meso-origami: folding multilayer graphene sheets.* Applied physics letters, 2009. **95**(12): p. 123121.
83. Detcheverry, F.A., et al., *Monte Carlo simulations of a coarse grain model for block copolymers and nanocomposites.* Macromolecules, 2008. **41**(13): p. 4989-5001.
84. Nielsen, S.O., et al., *Coarse grain models and the computer simulation of soft materials.* Journal of Physics: Condensed Matter, 2004. **16**(15): p. R481.

85. Plimpton, S., *Fast parallel algorithms for short-range molecular dynamics.* Journal of computational physics, 1995. **117**(1): p. 1-19.
86. Humphrey, W., A. Dalke, and K. Schulten, *VMD: visual molecular dynamics.* Journal of molecular graphics, 1996. **14**(1): p. 33-38.
87. Koh, S., et al., *Molecular dynamics simulation of a solid platinum nanowire under uniaxial tensile strain: Temperature and strain-rate effects.* Physical Review B, 2005. **72**(8): p. 085414.
88. Ni, R. and R. Adams, *The damping and dynamic moduli of symmetric laminated composite beams—theoretical and experimental results.* Journal of Composite Materials, 1984. **18**(2): p. 104-121.
89. Wachtman Jr, J., et al., *Exponential temperature dependence of Young's modulus for several oxides.* Physical review, 1961. **122**(6): p. 1754.
90. Dewapriya, M. and R.E. Miller, *Molecular dynamics study of the mechanical behaviour of ultrathin polymer–metal multilayers under extreme dynamic conditions.* Computational Materials Science, 2020. **184**: p. 109951.
91. Dewapriya, M. and R. Miller, *Molecular dynamics study of the penetration resistance of multilayer polymer/ceramic nanocomposites under supersonic projectile impacts.* Extreme Mechanics Letters, 2021. **44**: p. 101238.
92. Zhan, J., X. Yao, and X. Zhang, *Shock response of metal-ceramic nanolayered composites.* Composites Part B: Engineering, 2020. **199**: p. 108272.
93. Demaske, B.J., et al., *Atomic-level deformation of Cu x Zr100-x metallic glasses under shock loading.* Journal of Applied Physics, 2018. **123**(21): p. 215101.
94. Brown, H. and I. Ward, *Craze shape and fracture in poly (methyl methacrylate).* Polymer, 1973. **14**(10): p. 469-475.
95. Rottler, J., S. Barsky, and M.O. Robbins, *Cracks and crazes: on calculating the macroscopic fracture energy of glassy polymers from molecular simulations.* Physical review letters, 2002. **89**(14): p. 148304.
96. Meng, Z., et al., *Predicting the macroscopic fracture energy of epoxy resins from atomistic molecular simulations.* Macromolecules, 2016. **49**(24): p. 9474-9483.